1. COVER PAGE DATA ELEMENTS:

a. Federal Agency and Organization Element to Which Report is Submitted
U.S. DOE/NETL National Energy Tech Lab

b. Federal Grant or Other Identifying Number Assigned by Agency
Award no: DE-FE0030456

c. Project Title
Applying Anodic Stripping Voltammetry to Complex Wastewater Streams for Rapid Metal Detection

d. PD/PI Name, Title and Contact Information (e-mail address and phone number)
David Jassby
Associate Professor
Department of Civil and Environmental Engineering, UCLA
Email: jassby@ucla.edu
Phone: 310 – 825-1346

e. Submission Date
05/24/2021

f. DUNS Number
092530369

g. Recipient Organization (Name and Address)
University of California, Los Angeles
420 Westwood Plaza
5731 Boelter Hall
Los Angeles, CA 90095

h. Project/Grant Period
08/01/2017 – 07/31-2021

i. Reporting Period End Date
07/31/2021

j. Report Term Frequency
Final Report

1.Objectives

The overall objective of this project is the development of a lab-on-a-chip (LOC) electrochemical sensor capable of accurately measuring heavy metal (lead (Pb), cadmium (Cd), and arsenic (As)) concentrations in complex aqueous streams such as wastewater. The specific goals include: i) identify how heavy metal speciate and transform during the different stages of the wastewater treatment train, and explore pre-treatment methods that will de-complex heavy metals, making them available to ASV, ii) develop appropriate electrodes for ASV using organic/inorganic nanomaterials, and iii) integrate pre-treatment steps and specialized electrodes into an LOC sensor device capable of autonomously determining heavy metal concentrations in complex wastewater streams.

2.Tasks finished overview

2.1 Characterize Metal Speciation in Different Synthetic Wastewater

In this task, we have evaluated how different wastewater characteristics impact the speciation and form of heavy metals (Pb, Cd, and As). In addition, we explored how different wastewater treatment steps impact the speciation and form of these metals, with the goal of transforming these metals into species that are easily quantified using ASV.

2.2 Fabricate and Test Electrodes for ASV

In this Task, we have fabricated a range of electrode materials tailored towards the specific detection of Pb, Cd, and As. The electrode materials have been characterized for their structure by spectroscopy (UV-vis, FTIR, Raman and XRD), microscopy (SEM and TEM) and calorimetry (TGA and DSC) to look into the phase, morphology and defects.

2.3 Identify Pretreatment Methods for Metal Detection using ASV

In this Task, we have applied different pre-treatment steps to wastewater samples that were used in Task 2.1 to identify metal speciation. In addition, we have applied ASV to wastewater that was pre-treated to determine how this measurement method responds to the degree of pre-treatment.

2.4 Construct and Test ASV Device

We have fabricated ASV device, which is based on Python and Arduino.

3.Results and discussions

3.1 Characterize Metal Speciation in Different Synthetic Wastewater

3.1.1 Evolution of metal size distribution in synthetic wastewater throughout the WWTT

To investigate the mass of heavy metals associated with the different size fractions, we used 0.45 μm membranes and 5 kDa membranes to fractionate water samples into particulate (retentate from 0.45 μm membranes), colloidal (permeate from 0.45 μm membranes that is rejected by 5 kDa membranes), and dissolved fractions (permeate from 5 kDa membranes). Control experiments (i.e., filtration experiments performed with DI water and DI water spiked with heavy metals) showed that 19% ± 6% of water was lost during 5 kDa filtration process, which was due to low flux and enhanced water evaporation rates under vacuum conditions.

Figure 1 shows the relative amount of heavy metals in each size fraction from synthetic wastewater as a function of the treatment step. The behavior of Pb and Cd in synthetic raw wastewater varied significantly with As(III). 31% ± 6% of Pb and 20% ± 2% of Cd was found associated with the particulate fraction (i.e., >0.45 μm) in synthetic raw wastewater (Figure 1A-B). The percentage of Pb associated with the particulate fraction in synthetic raw wastewater was lower than that reported in real wastewater samples.[1, 2] We speculate that the high concentration of humic acid in our synthetic raw wastewater leads to the stabilization of Pb, keeping it in the colloidal fraction and preventing its sorption onto particulate matter.[3] The percentage of Cd in the particulate fraction found in synthetic raw wastewater (~20%) was in agreement with results reported by others,[1, 4] where 16% of Cd was found associated with the particulate form.[1] The 5 kDa membranes rejected almost all Pb and Cd from the synthetic raw wastewater, indicating that little Cd or Pb was in the dissolved fraction (i.e., < 5 kDa) in the synthetic raw wastewater (Figure 1A-B). However, the case for As(III) was quite different, with both the 0.45 μm membranes and 5 kDa membranes failing to reject As(III) from the synthetic raw wastewater or from effluent from any of the treatment steps (i.e., primary effluent and secondary effluent), indicating that nearly all As(III) was in the dissolved fraction and As(III) did not associate with any particulate or colloidal material throughout the WWTT (Figure 1C). The different behavior of As(III) and Pb/Cd are likely due to their different charges. Pb and Cd exist as cations in wastewater, which are readily sorbed by particles or colloids in synthetic raw wastewater that were rejected by the membranes. Other studies have also reported strong electrostatic attractive forces between Pb/Cd and humic acid.[5] However, it is difficult for these colloids and particles to adsorb As(III), which is typically found as H_3AsO_3 (with a pKa of 9.23 at 25 ℃),[6] a neutral molecule in the synthetic wastewater (pH = 7.16).

This weak interaction between As(III) and humic acid was also observed in other studies. For example, the presence of humic acid had little impact (< 2%) on the adsorption of As(III) by Fe-Mn oxides.[7] In addition to adsorption caused by electrostatic forces, acid-base interactions play an important role in the adsorption of metals on the surface of iron oxides.[8]

The impacts of flocculation on the metal size distribution depend on the metal species. Flocculation with $FeCl_3$ followed by sedimentation removed all of the Pb (~100% ± 0%) and over half of the As(III) (70% ± 2%) from the raw wastewater. To investigate the amount of Pb in different fractions of primary effluent, we spiked Pb into the stream. A large amount (~62% ±9%) of Pb was found in the particulate fraction (Figure 1A). This is likely because Pb is readily sorbed onto iron particles (i.e., $Fe(OH)_3$ flocs)[9] remaining in the flocculation effluent. Furthermore, during the size-distribution characterization process, a cake layer containing iron residues formed on the surface of the 0.45 μm membranes, which could adsorb Pb[9] and result in an overestimation of particulate Pb. Unlike Pb, only a modest amount of Cd (~33% ±13%) was removed by flocculation/sedimentation, which is consistent with literature reporting that flocculation/sedimentation is not effective at removing Cd.[10] In the primary effluent (i.e., effluent from the flocculation/sedimentation), 87% ± 5% of Cd existed in the dissolved phase (<5 kDa) (Figure 1), which is much higher than the fraction of dissolved Cd in raw wastewater (~13% ± 4%). This is likely because flocculation removed most of the humic acid, enabling any residual Cd to persist in the dissolved fraction.

The activated sludge process (i.e., secondary treatment) removed a large amount of Cd (~80%

± 7%), a modest amount of Pb (~40% ± 3%), and little As(III) (~0% ± 10%), which is in line with previous literature.[11] The removal of metals in the activated sludge process is influenced by many factors, including initial heavy metal concentrations, chemical oxygen demand in the effluent, sludge age, and extracellular polymers (ECPs).[12] ECPs play an important role in metals removal.[13] The higher removal of Cd compared to Pb is likely because of the stronger interactions between ECPs and Cd, compared to those between ECPs and Pb.[14, 15] In the secondary effluent, Cd and Pb showed similar behavior in terms of their partitioning to the various size fractions (Figure 1). The fractions of colloidal Pb and Cd in the secondary effluent were lower than those observed in raw wastewater, while the fractions of dissolved Pb and Cd in the secondary effluent were higher than those in raw wastewater, indicating that dissolved metals are more difficult to be removed during the activated sludge process than those in the particulate fraction.

Overall, in the presence of humic acid (e.g., in synthetic raw wastewater and synthetic secondary effluent), half of the Pb and Cd were found in the colloidal fraction (5 kDa - 0.45 μm). When humic acid was removed by flocculation, Pb was primarily found in the particulate fraction (> 0.45 μm), while Cd was primarily found in the dissolved fraction (< 5 kDa). The majority of As(III) was found in the dissolved fraction (< 5 kDa) and the WWTT had little impact on its size distribution.

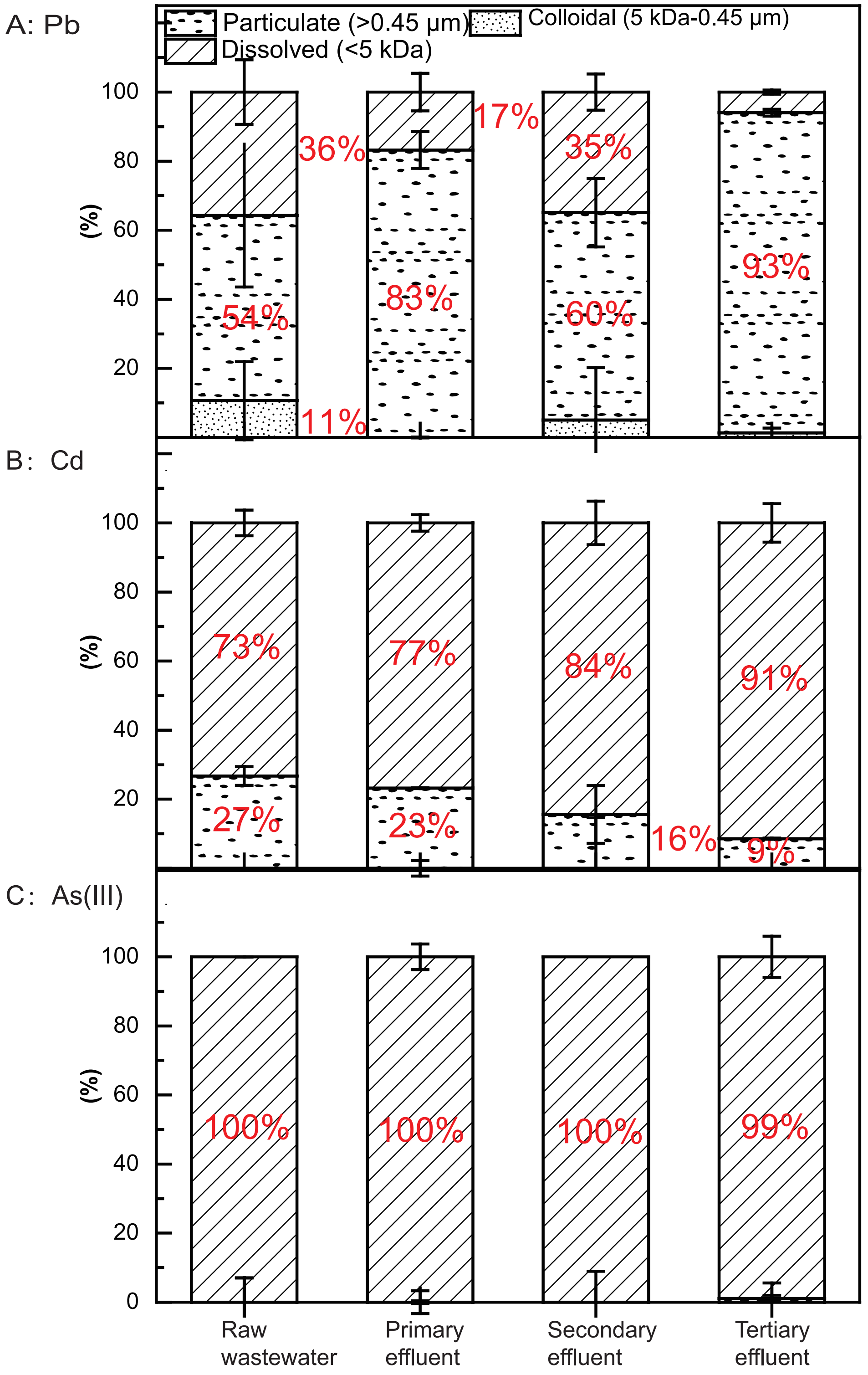

Figure 1. The relative amount of A) Pb, B) Cd and C) As(III) associated with particulate (>0.45 μm), colloidal (5 kDa-0.45 μm), and dissolved (<5 kDa) fractions of synthetic wastewater at different stages of the WWTT. The feed water for flocculation treatment and secondary treatment was synthetic raw wastewater. Fractions <5% are not labelled in the figure.

3.1.2 Evolution of metal partitioning in synthetic wastewater during the WWTT

Heavy metals in the colloidal and dissolved fractions are generally more difficult to remove compared to those in the particulate fraction. Therefore, it is useful to investigate the evolution of heavy metal partitioning in the colloidal and dissolved fractions. To investigate this, we dried permeate from the 0.45 μm membranes and applied the sequential extraction method. It is worth noting that the results shown here demonstrated heavy metal distribution under rather extreme conditions, where metals were “forced” to complex during the drying process.

Figure 2A shows the evolution of Pb partitioning in synthetic wastewater throughout the WWTT. In synthetic raw wastewater, the amount of Pb bound to NOM (~42% ± 7%) was similar to the Pb bound to iron or manganese oxides (~38% ± 4%) (Figure 2A). Interestingly, the distribution of non-particulate (i.e., colloidal and dissolved) Pb in this study was similar to the distribution of particulate Pb reported by Venkateswaran et al.,[16] indicating that size had little impact on the Pb partitioning. The distribution of Pb in primary effluent was not reported here because little Pb was detected in that stream. The Pb partitioning in secondary effluent was similar to its partitioning in raw wastewater, indicating that the activated sludge process had little impact on Pb partitioning behavior. Over half of Pb (~51% ± 1%) was bound to residues (i.e., the part of the sample that could only be digested by aqua regia at high temperature) in primary sludge, and 43% ± 1% of it was bound to NOM, indicating that Pb is highly stabilized in primary sludge. The partitioning of Pb in secondary sludge varies greatly between samples acquired from different wastewater treatment plants.[17] In our study, Pb in secondary sludge was primarily bound to metal oxides (49% ± 1%), with some Pb bound to the organic fraction (24% ± 1%), and a similar amount bound to carbonates (25% ± 2%) (Figure 2a). Overall, the WWTT had little impact on the Pb partitioning in synthetic waster.

Figure 2B shows the evolution of Cd partitioning in synthetic wastewater throughout the WWTT. Although Cd carries a similar charge to Pb, little Cd was bound to NOM and iron oxides in synthetic raw wastewater (Figure 2B), which was significantly different from Pb. Half of Cd existed as ions in synthetic raw wastewater (Figure 2B), indicating that Cd is much more mobile than Pb. This high mobility of Cd was confirmed by experiments with extended extraction time. After 6 hours of extraction with 1 M $MgCl_2$, most (~88% ± 3%) of the Cd was released as ionic Cd, while only 7% ± 7% of the Pb was released as ionic Pb. The mobility of Pb and Cd is in line with observations in MWW sludges[18] and soil samples.[19] The high mobility of Cd is likely because the stability constant of Pb/humic acid is much higher than that of Cd/humic acid.[20] The fraction of ionic Cd in primary effluent was much higher than that in raw wastewater, which likely resulted from the increased ionic strength since increased ionic strength could screen attractive forces between positive cadmium ions and negative substances.[21] In contrast to the partitioning of Cd in raw wastewater and primary effluent, over half of the Cd was bound to carbonate in secondary effluent. This is likely because the biological treatment process removed carboxylic acids (TOC decreased by approximately 90% after bio-treatmen) in synthetic wastewater, which led to an increase in the pH of the extraction solution (from 6.5 in raw wastewater ionic extraction solution to 9.6 in secondary effluent ionic extraction solution), causing the precipitation of Cd as carbonates. These precipitates would dissolve during the carbonate-fraction extraction process, manifesting Cd as bound to carbonate (Figure 2B). In primary sludge, over half of Cd (~67% ± 10%) was bound to the residues, which is similar to Pb, indicating that both Cd and Pb were both stable in primary sludge. In secondary treatment sludge, the fraction of ionic Cd was similar to the fraction of Cd bound to iron oxides. These two fractions accounted for most of the Cd, indicating that Cd was still mobile in secondary treatment sludges. However, it was reported that Cd partitioning varied significantly with sludge samples obtained from different sewage treatment plants.[17] Overall, flocculation enhanced ionic Cd concentrations, while secondary treatment increased carbonate-bound Cd in synthetic wastewater.

Most (~79% ± 5%) of the As(III) existed as free arsenic in synthetic wastewater (Figure 2C). This is because it is difficult for colloids or particles in wastewater to adsorb As(III), which has a Pka_1 of 9.23 at 25 ℃[6] and was predominantly present in its neutral form in our study (i.e., pH = 6.49 in ionic-extraction solution). Flocculation/sedimentation removed approximately 70% ± 2% of As(III), which agrees well with previous literature.[22] This high removal is because As(III) could form inner-sphere surface complexes with ferric hydroxides,[23] which is confirmed by the fact that most of the As(III) was found bound to iron oxides in primary effluent (Figure 2C). In primary sludge, over half (~54% ± 1%) of the As(III) was bound to residues, confirming that iron-based flocculation/sedimentation is a robust method to stabilize As(III). Unlike the behavior of As(III) in raw wastewater, over half (~70% ± 1%) of the As(III) was bound to carbonate in secondary effluent. However, we speculate that most of As(III) was ionic in secondary effluent because almost all As(III) was found in the dissolved fraction (Figure 1C). For the same reasons mentioned earlier, the overestimation of As(III) bound to carbonate was likely caused by an increase of pH in the ionic extraction solution, which could convert As(III) to its charged form that formed precipitates with magnesium,[24] presenting as As(III) bound to carbonate. We speculate that the conversion of As(III) to arsenate (As(V)) during the aerobic biodegradation process[25] also contributed to the large fraction of arsenic bound to carbonate because it is predicted that As(V) preferentially binds with carbonate compared to As(III).[26] In secondary sludge, little As(III) was bound to NOM or residue (Figure 2C), indicating that As(III) is highly mobile in secondary sludge. The high mobility of As(III) reported here agrees well with As(III) behavior reported in lake sediments.[27] Overall, secondary treatment had little impact on the partitioning of As(III), while flocculation with $FeCl_3$ significantly elevated the fraction of As(III) bound to iron oxides in synthetic wastewater.

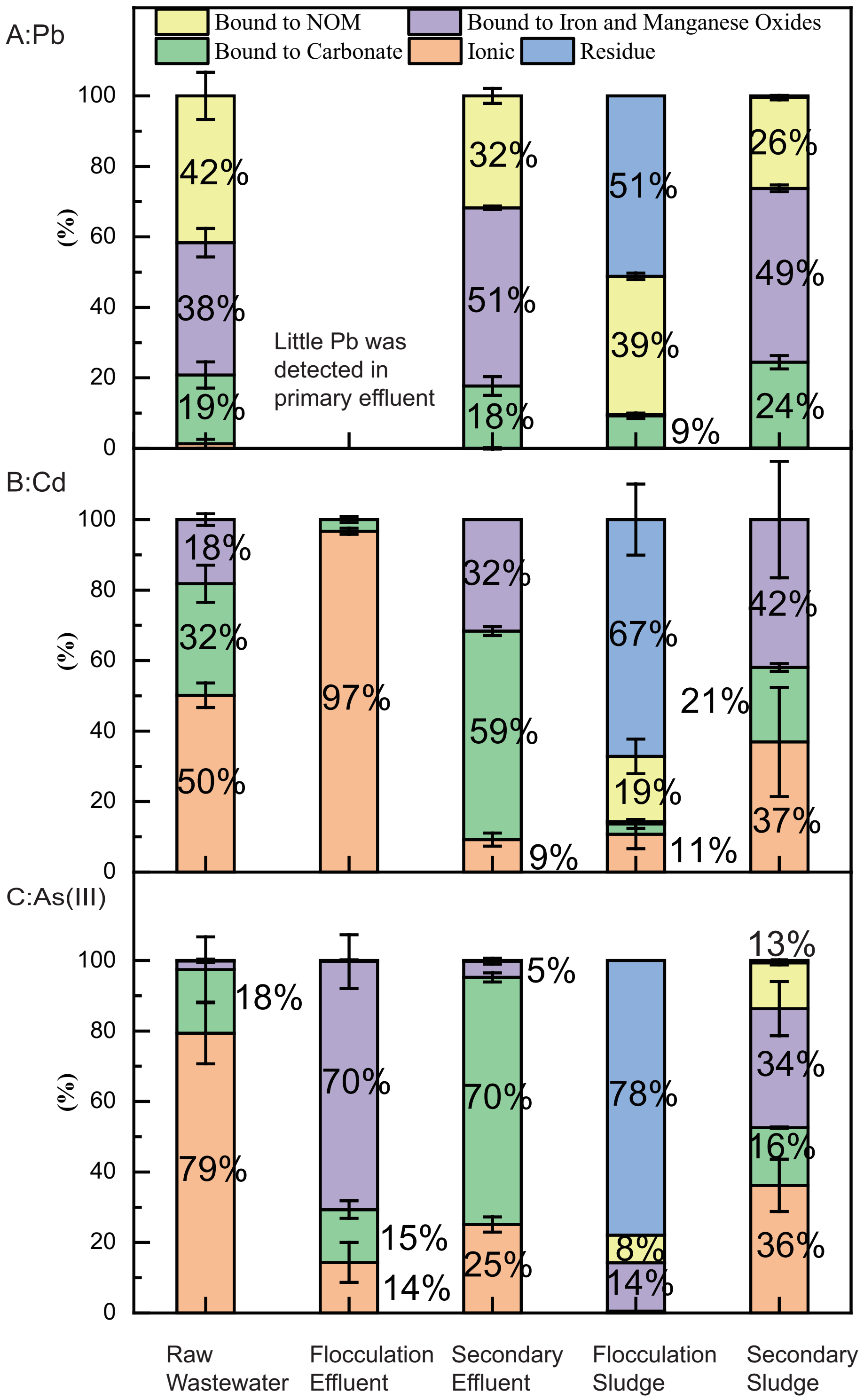

Figure 2. The evolution of A) Pb, B) Cd and C) As(III) partitioning in the colloidal and dissolved fractions (i.e., <0.45 μm) of synthetic wastewater throughout the WWTT. For effluent samples, permeate from 0.45 μm membranes was dried and extracted. Sludge samples were firstly centrifuged, then the residues were dried. The feed water for flocculation treatment and

secondary treatment was raw wastewater. Fractions <5% are not labelled in the figure.

3.1.3 Influence of hardness on distribution of metals

Water hardness plays an important role in heavy metal behavior such as metal solubility[28] and sorption.[29] To investigate the impacts of water hardness on the distribution of heavy metals in wastewater, experiments were performed in soft (60 mg/L hardness as $CaCO_3$), hard (127 mg/L hardness as $CaCO_3$), and very hard (200 mg/L hardness as $CaCO_3$) synthetic wastewater. Figure 3 shows the influence of an increased hardness on the amount of metals in the different wastewater fractions. The elevated hardness had little impact on the particulate fraction of Pb and Cd. However, an increase in hardness resulted in an increase of Pb and Cd in the dissolved fraction (Figure 3). This increased dissociation of metals from metal-humic complexes resulting from an increase of divalent ions was also observed by previous researchers.[30] This is likely caused by an increase in ionic strength that compresses the electrical double layers of the particles,[21] which limits the effectiveness of electrostatic attractive forces between cations (i.e., metals) and colloids. As a result, it reduced the possibility of metals to interact with colloids,[30] and increased the percentage of dissolved metals. Furthermore, the limited effectiveness of electrostatic repulsive forces between colloids would promote their aggregation and reduce the effective surface area, thus boosting the percentage of dissolved metals. Water hardness had little impact on the partitioning of metals in synthetic wastewater, as the percentage of different fractions of metals in different hardness conditions were nearly identical across all hardness values (Figure 4).

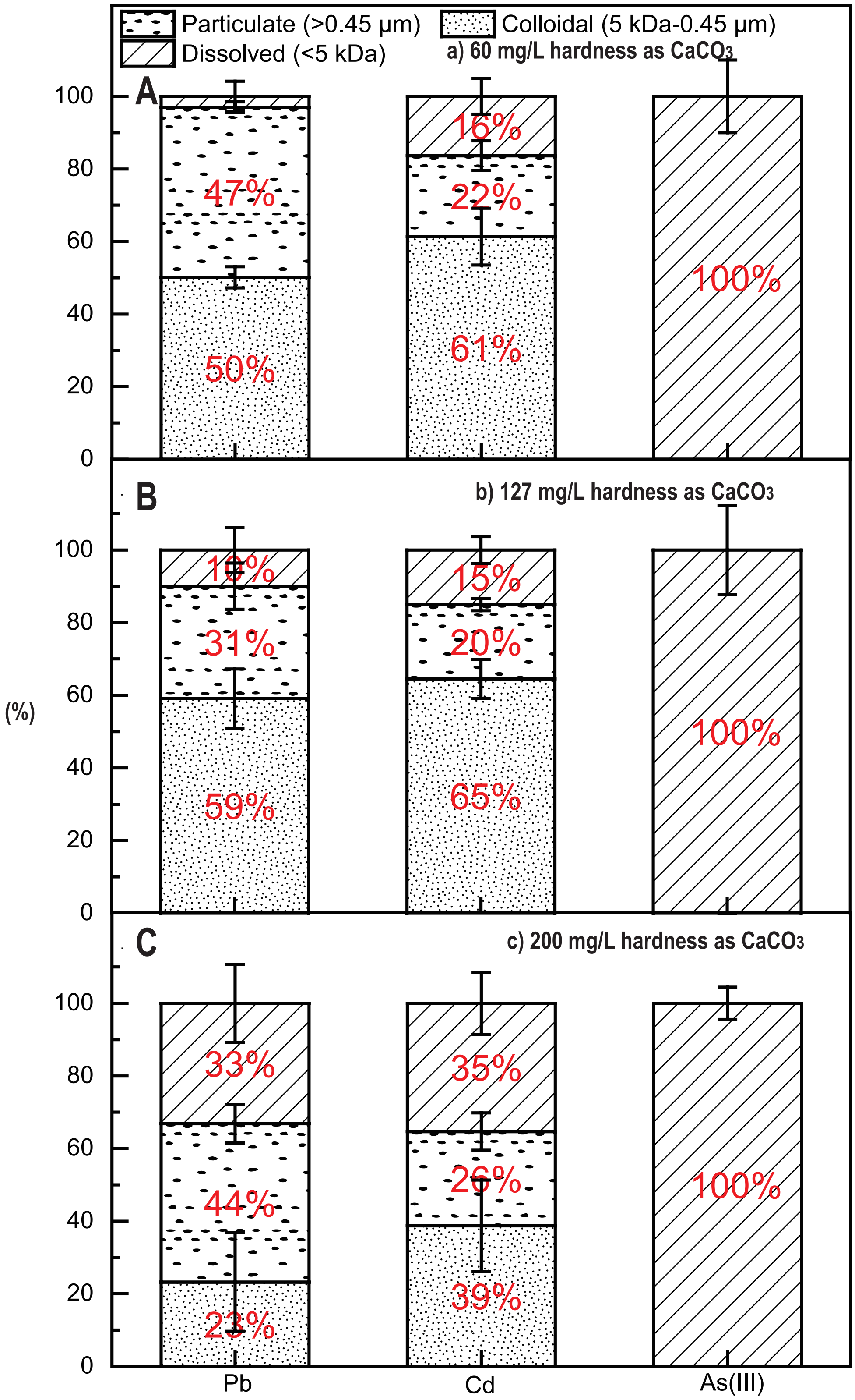

Figure 3. Influences of hardness as A) 60 mg/L B) 127 mg/L C) 200 mg/L $CaCO_3$ on size distribution of heavy metals in particulate (>0.45 μm), colloidal (5 kDa-0.45 μm), and dissolved

fractions (<5 kDa) of synthetic raw wastewater. Fractions <5% are not labelled in the figure.

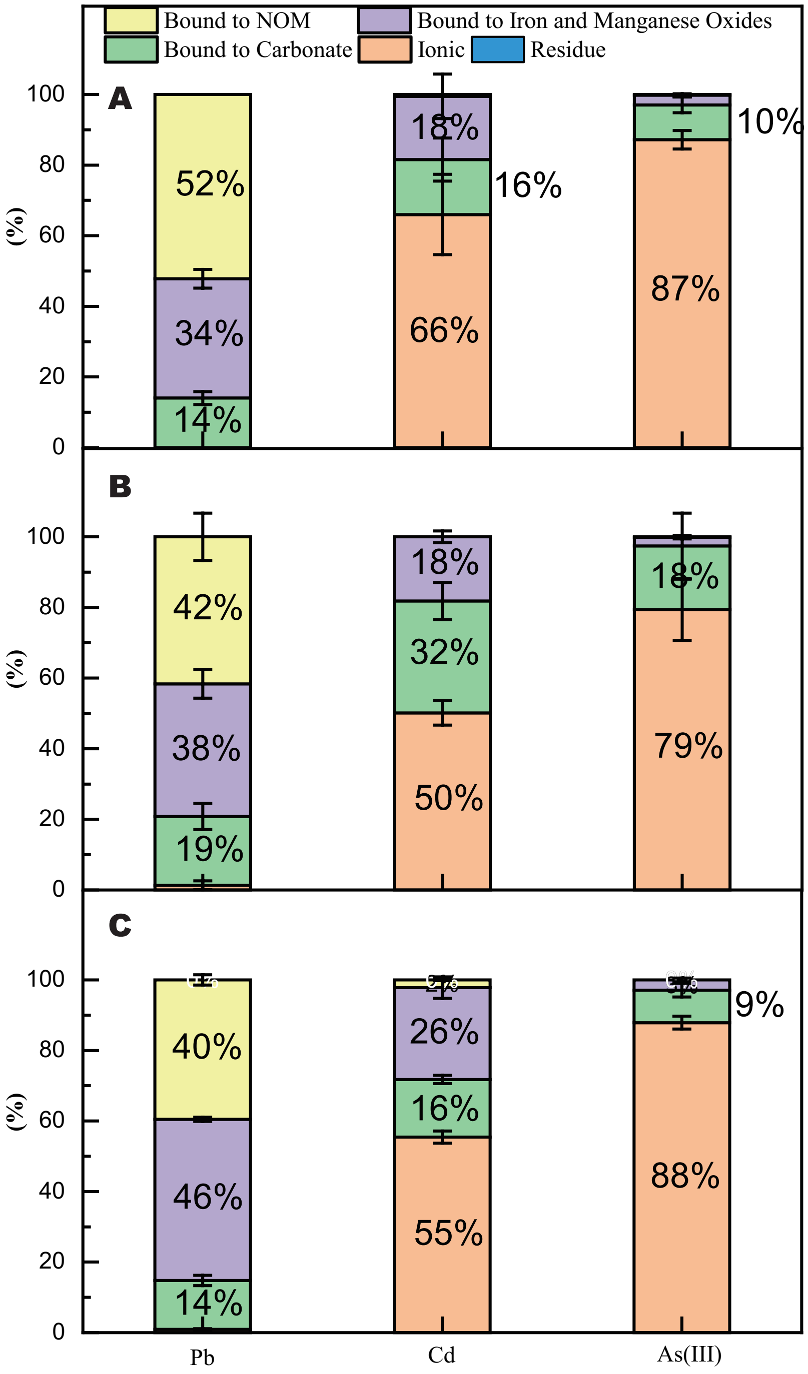

Figure 4. Influences of hardness as A) 60 mg/L B) 127 mg/L C) 200 mg/L $CaCO_3$ on partitioning of heavy metals in synthetic raw wastewater. Permeate from 0.45 μm membranes was dried and extracted. Fractions <5% are not labelled in the figure.

3.1.4 Evolution of metals in real wastewater samples

To verify the data obtained from synthetic wastewater, we investigated the evolution of metals in real wastewater. Figure 5 shows the relative amount of metals in particulate, colloidal, and dissolved fractions of real wastewater samples. The distribution of metals in real raw wastewater was similar to that in real primary effluent, indicating that physical treatment (i.e., sedimentation) had little impact on heavy metal size distribution. In real wastewater, Pb was primarily found associated with the particulate fraction (54%~93%) (Figure 5), which is in line with previous reports.[1] However, in synthetic wastewater, Pb was primarily (38%~59%) found in the colloidal fraction (Figure 1). We speculate that this difference is caused by a relatively high concentration of humic acid in the synthetic wastewater, which can complex with Pb[30] and prevent it from being sorbed onto larger particles.[3] A large amount of Pb was associated with the particulate fraction in real tertiary treatment effluent, which is a chemically enhanced filtration process (i.e., a coagulant is added before filtration). A similar high fraction of particulate Pb was also observed in synthetic wastewater flocculation effluent (Figure 1A); in both cases, FeCl3 was used as the coagulant. This is likely because Pb is sorbed onto residual iron particles in the coagulation effluent.[9] In addition, the cake layer containing iron residues on the surface of the 0.45 μm filters used for size fractionation may sorb non-particulate Pb, leading to an overestimation of particulate Pb.[31] A small fraction (< 30%) of Cd in real raw wastewater was found associated with the particulate fraction, which is in line with Cd behavior in synthetic raw wastewater and in the literature.[1] However, most of the Cd in real wastewater samples was in the dissolved fraction, which is different from the size distribution of Cd in synthetic wastewater, where most of the Cd was associated with the colloidal fraction. Again, this is likely caused by the relatively high concentration of humic acid in synthetic wastewater.[32] However, the interactions between Cd and humic acid are weaker[20] compared to Pb, and increased ionic strength could release Cd from humic acid (Figure 2).

Overall, the evolution of metal size distribution in real wastewater was similar to that observed in synthetic wastewater. Due to the low concentration of humic acid, Pb was primarily found in the particulate fraction, which was further increased by flocculation with $FeCl_3$. Cd was primarily found in the dissolved fraction, which gradually increased throughout the WWTT. Most of As(III) was found in the dissolved fraction, and the WWTT had little impact on it.

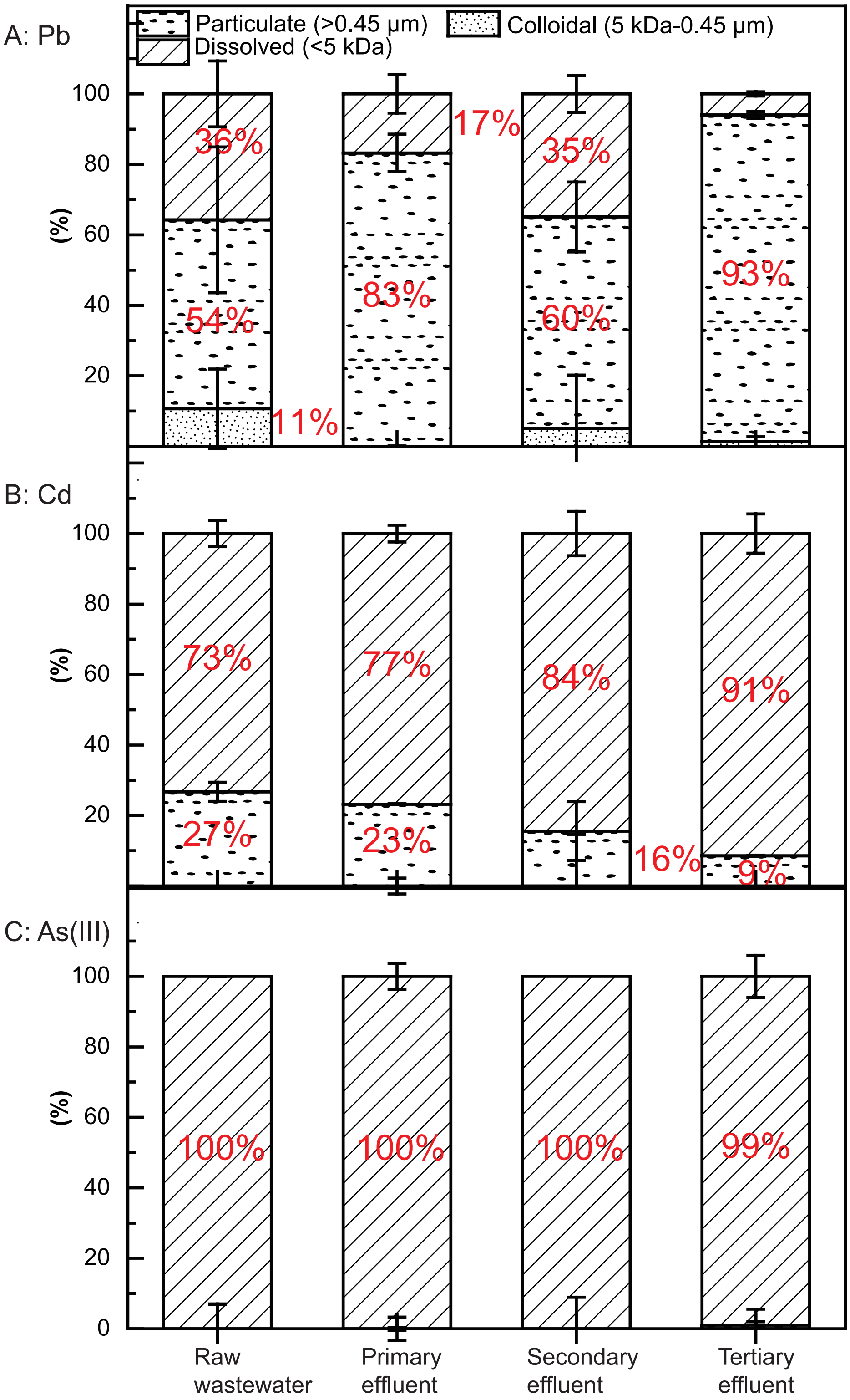

Figure 5. The amount of A) Pb, B) Cd and C) As(III) in particulate (>0.45 µm), colloidal (5 kDa-0.45 µm), and dissolved (<5 kDa) fractions of real wastewater samples throughout the WWTT. Fractions <5% are not labelled in the figure.

Figure 6 shows the evolution of heavy metal partitioning in real wastewater samples obtained from the different stages of the WWTT. The metal partitioning in raw wastewater was similar to that in primary effluent, indicating that physical treatment (i.e., sedimentation) had little impact on heavy metal partitioning. Although heavy metal partitioning in real wastewater samples was different from those observed in synthetic wastewater, the evolution of heavy metal partitioning throughout the WWTT in real wastewater samples was similar to that observed in synthetic wastewater. The majority of Pb was bound to carbonate (79% to 100%) in all real wastewater samples except in tertiary effluent, which is likely because the concentration of humic acid was low in this batch of real wastewater and few compounds competed with carbonate to complex Pb (log Ksp of $PbCO_3$ is -13.76 ± 0.15).[33] As expected, the fraction of Pb bound to iron oxides dominated in the tertiary (i.e., chemically enhanced filtration) effluent, confirming that Pb is readily sorbed by iron oxides.[30] In real raw wastewater samples, most of the Cd was ionic (~72%), which was similar to what was observed (~50%) in synthetic raw wastewater, confirming that Cd is highly mobile in wastewater. Like the results generated from synthetic wastewater, secondary treatment elevated the fraction of Cd bound to carbonate. As expected, tertiary treatment slightly increased the fraction of Cd bound to iron oxides, but otherwise did not dramatically change the partitioning of Cd. Surprisingly, most of the As(III) was bound to carbonate in real wastewater samples, which was significantly different from the distribution of As(III) in synthetic wastewater. We speculate that this is because the pH of ionic-extraction solution (i.e., 1 M $MgCl_2$) in real wastewater sample was high (i.e., pH = 9.18) because of the lack of acids, allowing As(III) to form precipitates with Mg.[24] These precipitates would dissolve during the carbonate extraction process because of the addition of acid, manifesting as As(III) bound to carbonate. In fact, most of As(III) was ionic, which is supported by the fact that the majority of As(III) was found in the dissolved fraction (Figure 5). Similar to As(III) behavior in synthetic wastewater, the fraction of As(III) bound to iron oxides increased in tertiary effluent, likely because arsenic can form inner-sphere complexes with iron oxides.[23] Overall, similar to Pb and As(III) in synthetic wastewater, the WWTT had little impact on their partitioning in real wastewater, except that flocculation with $FeCl_3$ caused the formation of metal/iron complexes; secondary treatment increased the fraction of Cd bound to carbonate.

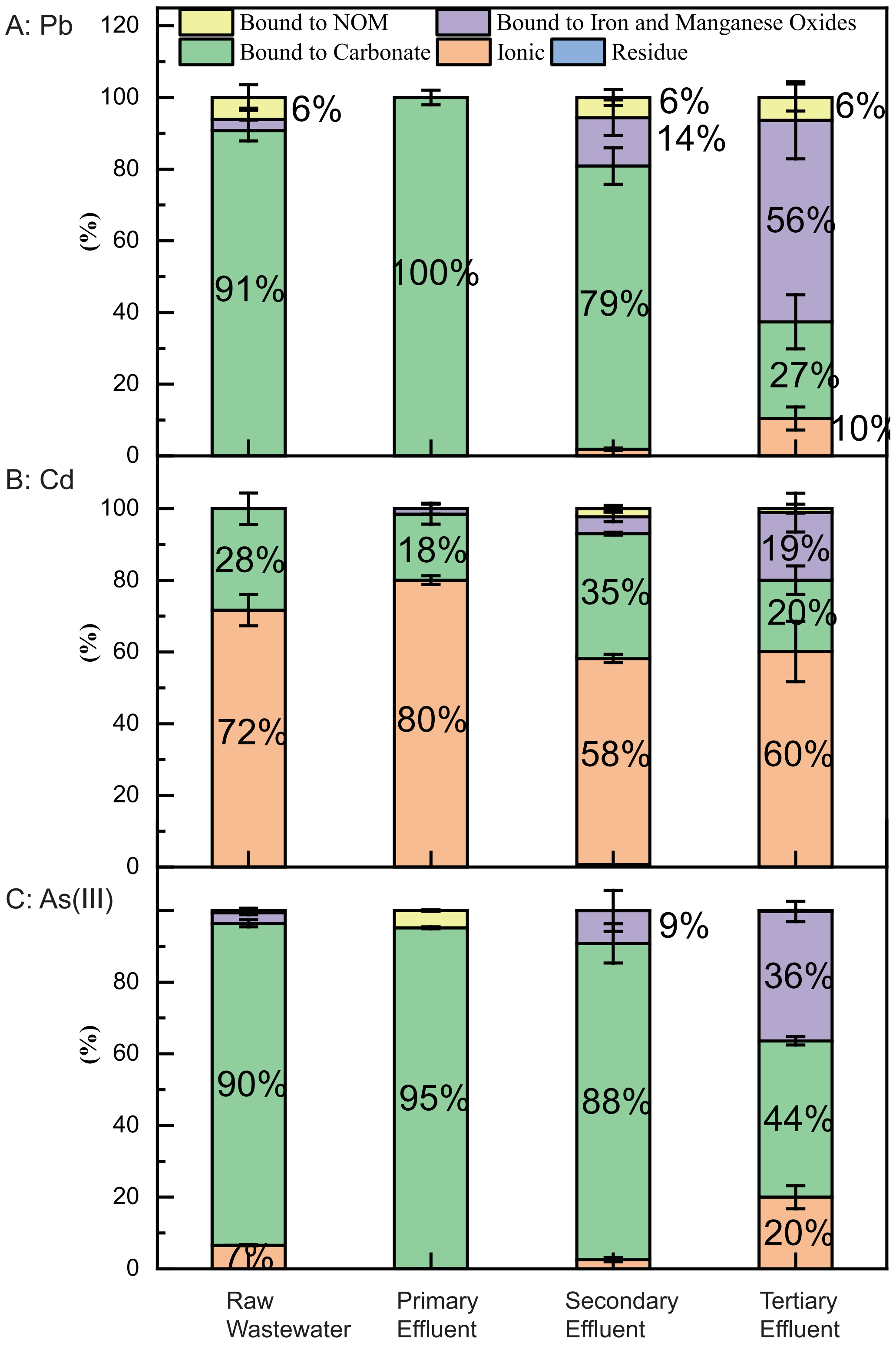

Figure 6. The evolution of A) Pb, B) Cd and C) As(III) distribution in real wastewater samples throughout the WWTT. Permeate from the 0.45 μm membranes was dried and extracted using the sequential extraction method. Fractions <5% are not labelled in the figure.

3.1.5 Summary of metal characterization

The evolution of metal size distribution and partitioning throughout the WWTT is of paramount importance for developing metal detection and metal removal techniques. The distribution of heavy metals in wastewater was dependent on the metal species, as well as water quality characteristics. For the different metals tested here, 57% of Pb and 65% of Cd were associated with humic acids in raw synthetic wastewater, which kept them in the 5 kDa – 0.45 µm fraction. The concentration of humic acid in real wastewater was much lower than that in synthetic wastewater. As a result, the majority (54%~93%) of Pb was found in the particulate (>0.45 µm) fraction, primarily associated with oxides and/or carbonate particles, while the majority (between 73% and 91%) of Cd was found in the dissolved (i.e., < 5 kDa) fraction. The WWTT had little impact on the size distribution of Pb, except that flocculation with $FeCl_3$ increased particulate Pb. In contrast, the WWTT gradually increased the dissolved Cd fraction. As(III) remained in the dissolved fraction, and the WWTT had little impact on its size distribution.

Importantly, the metal partitioning analysis presented here demonstrated the partitioning of metals in the colloidal and dissolved fractions (<0.45 µm) under extreme conditions driven by the drying step used during the extraction process, which forced metals to complex with other components of wastewater. Nearly half (~42%) of Pb was bound to humic acid, while half (~50%) of Cd was identified as ionic in raw synthetic wastewater. A similar partitioning behavior was observed for Cd in real raw wastewater. However, most of the Pb was bound to carbonates in real raw wastewater. The majority of As(III) was highly mobile in wastewater. The WWTT had little impact on the partitioning of Pb and As(III) except that flocculation with $FeCl_3$ caused the formation of metal/iron complexes. However, flocculation elevated ionic Cd, and the activated sludge process elevated Cd bound to carbonate. Generally, an increase of water hardness slightly increased the metal concentrations in the dissolved fraction, while it had little impact on their partitioning. Overall, this study provides information to plant operators and potential users of treated wastewater regarding the fate and speciation of heavy metals in municipal wastewater streams.

3.2 Fabricate and Test Electrodes for ASV

3.2.1 Fabrication and test of As(III) electrode

3.2.1.1 Physicochemical characterization of Fe_3O_4-Au nanocomposite

The introduced synthesis protocol is time-saving (1-2 h), as the synthesis of magnetite NPs was conducted using the co-precipitation method. It is also linker-free with no barrier between gold and magnetite, which improves the electron transfer between them and enhances their synergistic effects. This protocol uses simple chemicals that are mostly ecofriendly, and very easy to wash using deionized water, if any excess is present. In addition, magnetite nanoparticles were prepared to be very tiny (≈10 nm) to allow for higher surface area and higher adsorption of As(III). The morphology and sizes of the prepared particles were assessed using SEM & TEM imaging as illustrated in Fig. 7. The synthesized Fe_3O_4-Au suspension was drop casted as a thin film on a piece of silicon wafer, at the same concentration and volume used in preparing the electrode materials, and sputtered with Pd/Pt to reduce surface charging, and then imaged by SEM. The SEM image in Fig. 7a illustrates that AuNPs (the bigger and brighter particles) are surrounded by much smaller Fe_3O_4NPs. However, the Fe_3O_4NPs were not well resolved. Further imaging of Fe_3O_4-Au by TEM (Fig. 7b) shows a 70 nm spherical core AuNP decorated with Fe_3O_4NPs, which agrees with the SEM image. TEM image of Fe_3O_4NPs showed the particles are spherical with an average size of 10±3 nm (Fig. 7c & 7d). The TEM images confirm the success of the proposed platform, as the AuNPs and Fe_3O_4NPs are directly bound to each other without separation between them. Furthermore, EDX spectroscopy was implemented to calculate the actual weight ratio between Au and Fe in the prepared nanocomposite.

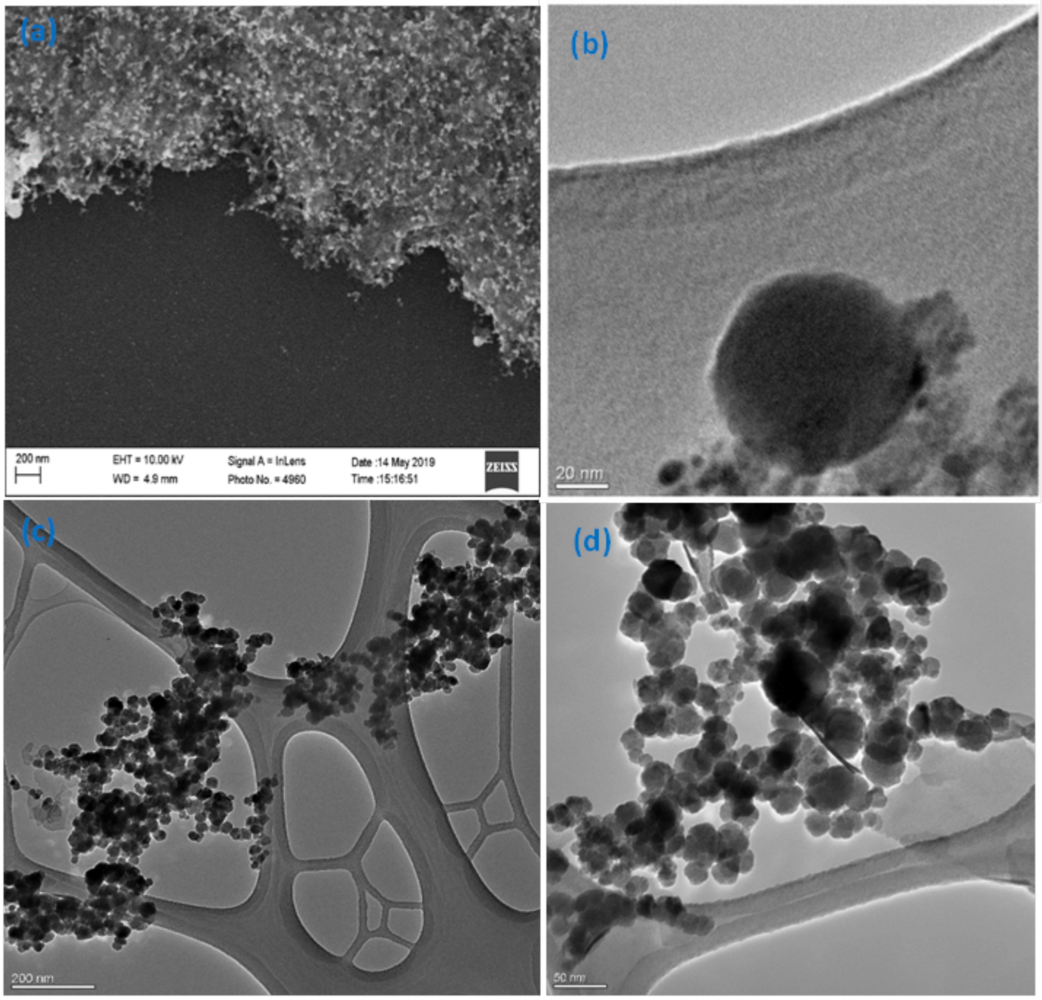

Figure 7**.** (a) SEM image of a thin film of Fe_3O_4-Au nanocomposite on a silicon wafer sputtered

with Pd/Pt, (b) a higher resolution TEM image of the prepared nanocomposite, and (c & d) TEM images of the Fe_3O_4NPs.

Results of the XRD analysis of magnetite (Fe_3O_4) NPs in Fig. 8 show diffraction peaks at 30.17°, 35.53°, 43.27°, 56.96°, 62.69°, which can be assigned to the (220), (311), (400), (511), and (440) planes of the cubic inverse spinel type structure of magnetite. Moreover, the diffraction pattern of Fe_3O_4-Au has the same peaks of magnetite addressed above in addition to the characteristic peaks of the face-centered cubic (FCC) AuNPs at 38.23°, 44.54°, 64.71°, 77.69°, which can be assigned to the (111), (200), (220), and (311) planes, (Pattern 4-784). Hence, the XRD data confirms the successful synthesis of the Fe_3O_4-Au nanocomposite, without any change in the magnetite phase. Moreover, the intensity of AuNPs peaks is higher because they are in a higher concentration, which agrees with the EDS data, in which the weight ratio is around 5:1 (Au:Fe). FTIR spectrum analysis (Fig. 8) of Fe_3O_4NPs shows a broad peak centering at 3380 cm^{-1} and two peaks at 2900 and 2915 cm^{-1}, which are attributed to the stretching vibrations of O-H and C-H groups from EG, respectively. In addition, Fe-O vibrations show two peaks at 1380 and 565 cm^{-1}. Vibration peaks of Fe_3O_4NPs are in a good agreement with published work. On the other hand, spectrum of AuNPs shows stretching vibrations of O-H groups of PVA at 3320 cm^{-1}, vibrations of C=O groups of sodium citrate at 1730 cm^{-1}, and stretching vibrations of C-H groups at 2900 and 2915 cm^{-1}. The FTIR spectrum of Fe_3O_4-Au contains all peaks from both spectra of Au and Fe_3O_4, which confirms the successful synthesis of this nanocomposite.

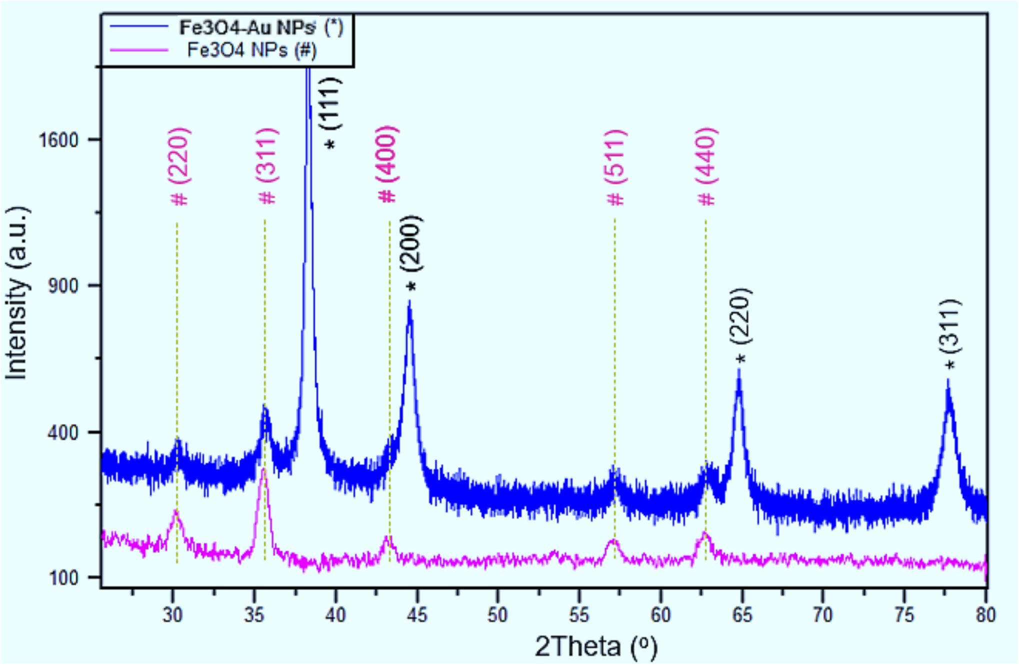

Figure 8. XRD patterns of Fe_3O_4NPs and Fe_3O_4-Au.

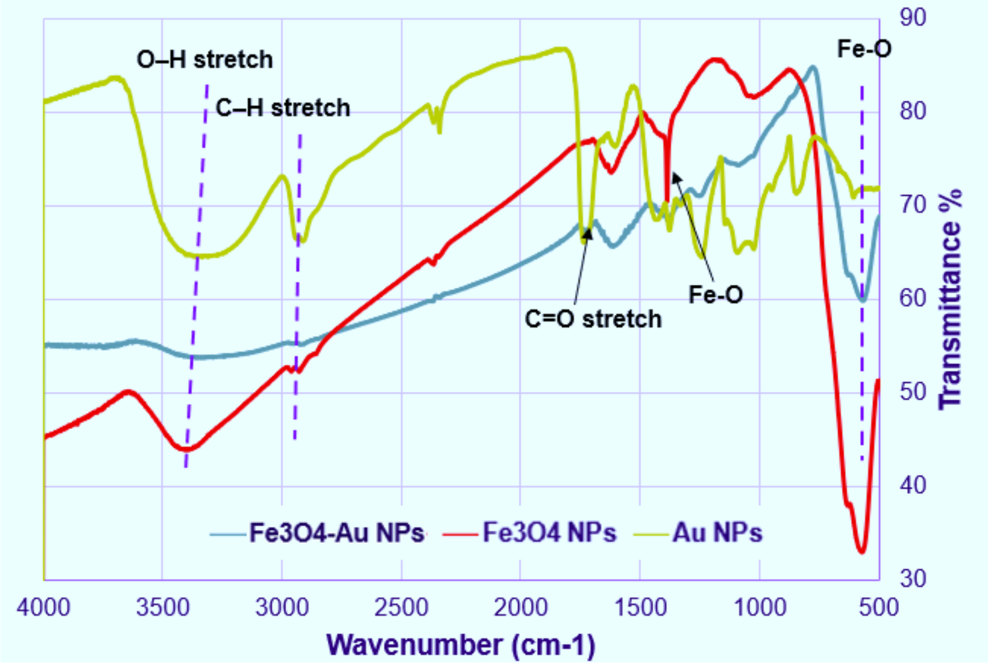

Fig. 9. FTIR spectra of Fe_3O_4, Au, and Fe_3O_4-Au.

The synthesis protocol introduced in this work can be used as a new platform for synthesis of intact metal-Fe_3O_4 nanocomposites without the need for any linkers, which minimizes the distance between the metal and metal oxide nanoparticles and ensures the optimum synergistic effects between the materials. In this protocol, EG could provide magnetite with hydroxyl groups that facilitate the chelation of Au ions (Fe_3O_4-Au^{3+}), as illustrated in the schematic diagram of Fig. 10. In this novel platform method, sodium citrate is a mild reducing and capping agent that can reduce gold ions slowly into AuNPs, while it will not reduce $Fe^{3+/2+}$ in magnetite and hence it enables the synthesis of the Fe_3O_4-Au nanocomposite *in situ* without any linkers.

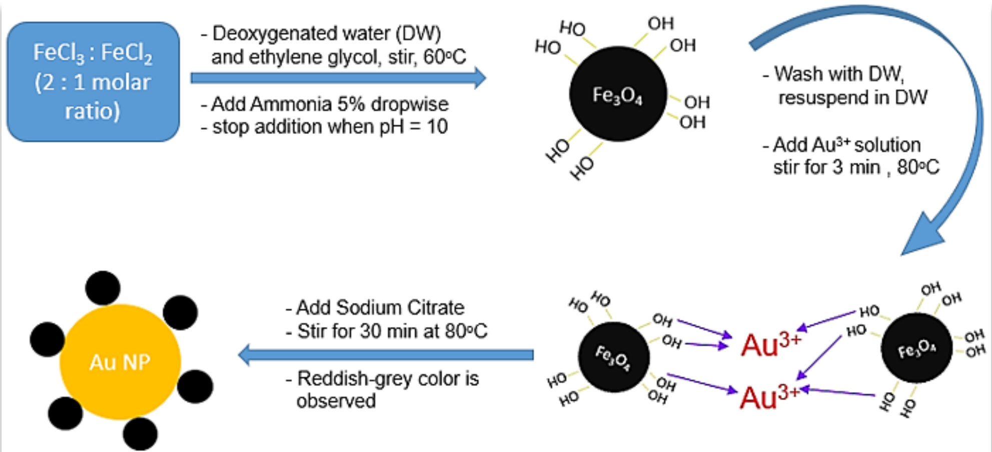

Figure 10. Schematic of Fe_3O_4-Au nanocomposite preparation and the suggested mechanism of its formation.

3.2.1.2 Sensitivity, limit of detection, and reproducibility

The Fe_3O_4-Au-IL/GCE operating at optimal Fe:Au mass ratio, deposition potential, and deposition time determined above, was applied to analyze 0 to 100 ppb of As (III) in 0.2 M pH 5 acetate buffer (Fig. 11). The results show well-defined Gaussian shaped response with peak current around 0 V which increased with increasing As(III) concentration (Fig. 11A). As illustrated in Fig. 11B, the peak stripping current, i.e. response, was linearly related to As(III) concentration over the complete concentration range of 0 to 100 ppb. The sensitivity (the slope of the calibration plot) was 0.122 mA/ppb As(III) and the LOD (calculated based on S/N = 3) was 0.22 ppb. The high sensitivity and low LOD is credited to the synergistic effects of excellent absorption ability for As(III), high electrical conductivity and good stability of AuNPs, Fe_3O_4 NPs and IL.

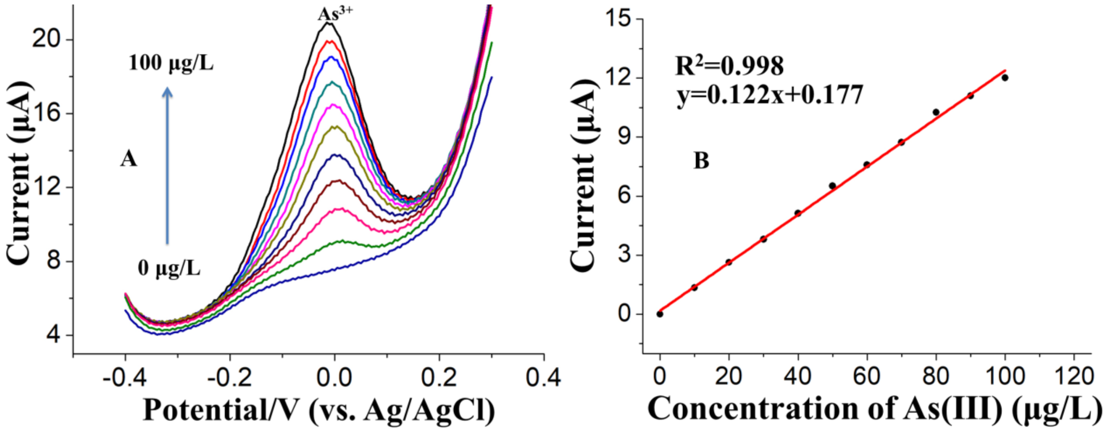

Figure 11. (A) SWAS voltammograms for additions of 0, 10, 20, 30, 40, 50, 60, 70, 80, 90 and 100 µg/L As(III). (B) The corresponding calibration curve of As(III).

3.2.1.3 Selectivity

Water sources contain a plethora of anions and cations that can potentially interfere in the SWASV detection of As(III). We investigated the interference on the analysis of 50 ppb of

As(III) from 100-fold higher concentrations of Na^+, K^+, Ca^{2+}, Zn^{2+}, Mg^{2+}, Mn^{2+} and Fe^{2+}, and a 150-fold higher concentrations of Cl^-, NO_3^-, SO_4^{2-}, CO_3^{2-}, F^- and PO_4^{2-}. As shown in Fig. 12, there were no measurable changes in the peak current signals (current variation < ± 10%) in the presence of all the tested ions, confirming the proposed Fe_3O_4-Au-IL/GCE is efficient in the detection of As(III) in presence of other interfering species in water.

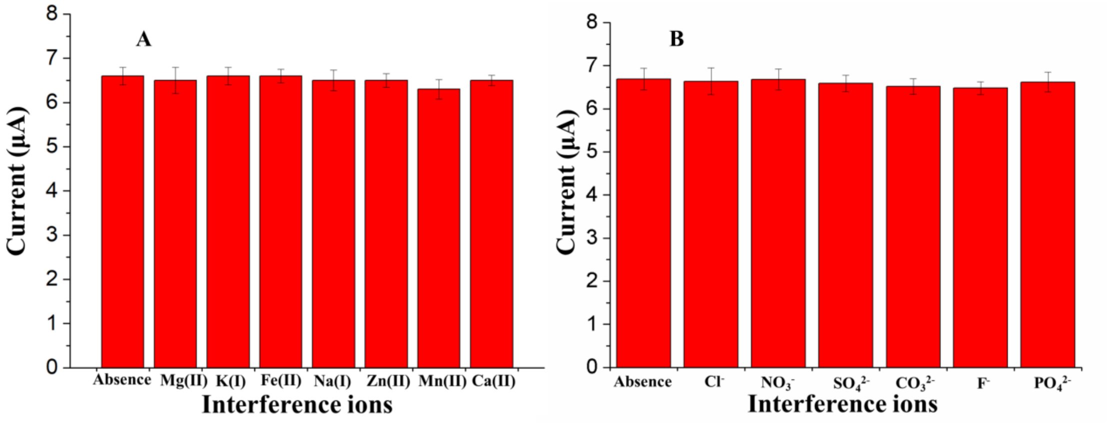

Figure 12. Interference study of high concentrations of different ions (A: Cation; B: Anion) on the stripping peak current of 50 μg/L As(III) at Fe_3O_4-Au-IL/GCE in 0.2 M acetate buffer (pH 5.0). Each data point is an average of 5 measurements from 3 electrodes and error bars represent ±1standard deviation.

3.2.2 Fabrication and test of Pb(II) and Cd(II) electrode

3.2.2.1 Characterization of $(BiO)_2CO_3$-rGO nanocomposite

The XRD analysis confirmed that the prepared nanocomposite was $(BiO)_2CO_3$-rGO (Figure 13A). The interplanar distance between graphene sheets in the hexagonal structure of graphite was d = 0.345 nm, corresponding to 2theta = 26° (Figure 13A),[34] while the oxidation process pushed the layers away and increased the interplanar distance to d = 0.743 nm, which corresponds to 2theta = 10.6° (Figure 13A). Regarding $(BiO)_2CO_3$-rGO (Figure 13A), the XRD peaks matched the diffraction peaks of the rhombohedral-phased bismuth (JCPDS card no. 05-0519). However, the two peaks at 30.02° and 32.66° didn't match the bismuth pattern. They match the (103) and (110) planes of the diffractogram $(BiO)_2CO_3$ (Natl. Bur. Stand., U.S.), and the starting materials of GO and EG could be the carbon sources for the formation of the sub-carbonate[35] Hence, the XRD analysis confirmed that the prepared nanocomposite was $(BiO)_2CO_3$-rGO.

FTIR confirmed the formation of $(BiO)_2CO_3$ and the addition of Nafion to the nanocomposite. The FTIR spectrum of GO nanosheets (Fig. 13B) synthesized by the modified IHM exhibited peaks of the following groups: O-H stretching vibration at 3420 cm^{-1}, overlapping with the broad peak of O-H from carboxyl groups from 2500 to 3500 cm^{-1}, C=O stretching vibrations at 1750 cm^{-1}, C=C from unoxidized SP^2 hybridized carbon atoms at 1620 cm^{-1}, and C-C vibrations at 1250 cm^{-1}, which is in line with the literature.[12] In addition, the recorded FTIR of the in-situ synthesized $(BiO)_2CO_3$-rGO nanocomposite (Figure 13B) showed disappearance of the broad peak of O-H groups at 2500-3500 cm^{-1}, confirming the reduction process.[36] The introduction of two new peaks at 873 & 1350 cm^{-1} can be attributed to the vibrations of carbonate,[37] which confirms the formation of $(BiO)_2CO_3$. Moreover, the addition of Nafion to the nanocomposite (Figure 13B) was confirmed by the $–SO_3–$ symmetric stretching vibrations peaks at 1056 cm^{-1} and asymmetric vibrations of $–SO_3–$ groups at 1201 cm^{-1}.[38] Figure 1C shows the Raman spectroscopic analysis of GO and $(BiO)_2CO_3$-rGO nanocomposite. Graphene materials showed two main peaks in Raman spectra. The first is the G-band that appeared around 1580 cm^{-1}, and the second is the D-band that appeared around 1350 cm^{-1}.

The G-band is attributed to the in-phase vibrations of the SP^2 lattice, while the D-band refers to the structural defects and disorders. The I_D/I_G ratio is around 0.1 in graphite (Figure 13C), 0.9 in GO (Figure 13C), and 1.2 in $(BiO)_2CO_3$-rGO (Figure 13C), which illustrates introducing lattice defects and decreasing the average size of the SP^2 domains by the oxidation process in GO, and more defects by reduction of GO into rGO.[39] These results of rGO matched the literature[40] and it can be attributed to eliminating the defects but at the same time introducing a higher number of new smaller graphitic domains. Moreover, the Raman bands at 100, 512, and 1070 cm^{-1} were attributed to the vibrations of bismuth subcarbonate.[41]

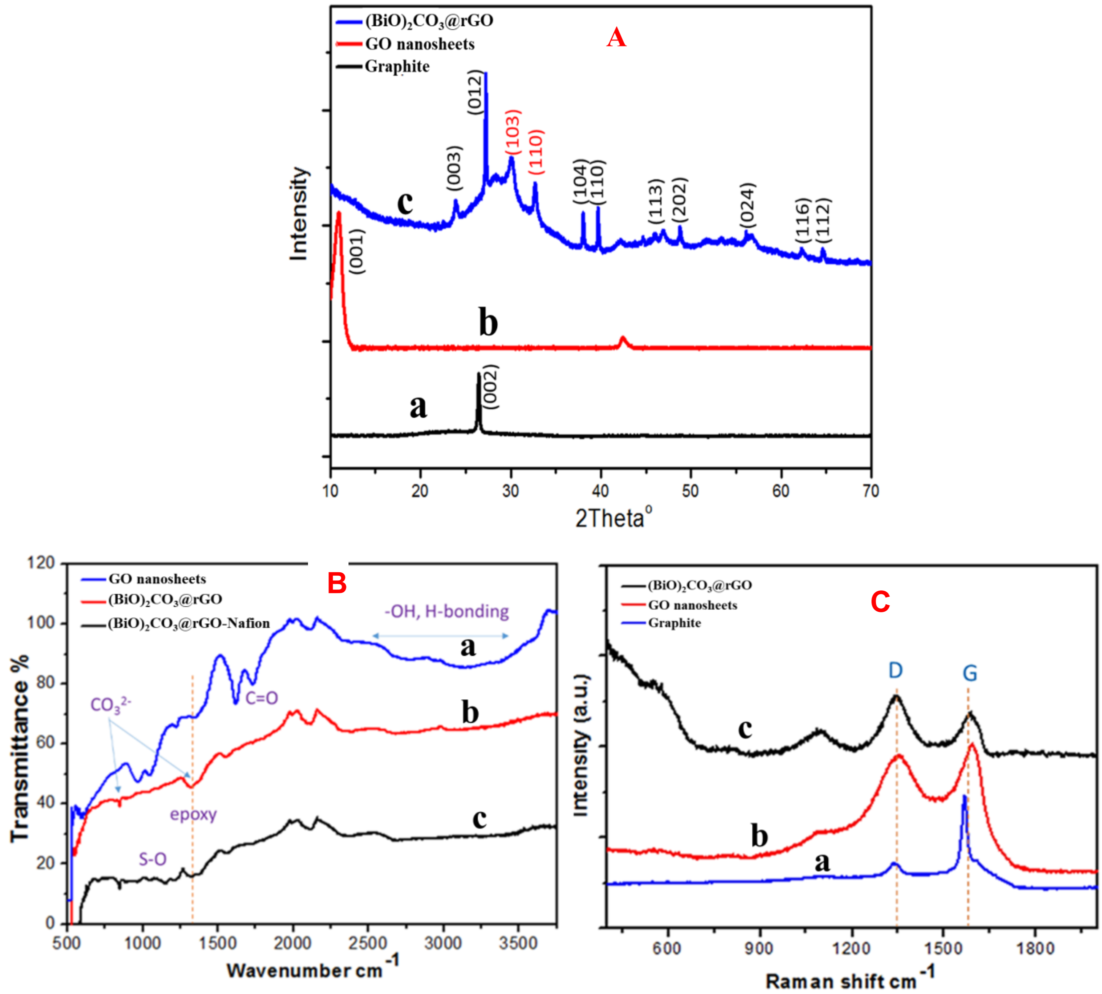

Figure 13. XRD analysis of Aa) graphite, Ab) GO and Ac) $(BiO)_2CO_3$-rGO nanosheets, FTIR spectra of Ba) GO nanosheets, Bb) $(BiO)_2CO_3$-rGO nanocomposite and Bc) $(BiO)_2CO_3$-rGO-

Nafion nanocomposite, and Raman spectra recorded at 514 nm laser beam of Ca) graphite, Cb) GO nanosheets, and Cc) $(BiO)_2CO_3$-rGO nanocomposite.

3.2.2.1 Performances of $(BiO)_2CO_3$-rGO-Nafion/GCE in DI water and synthetic river water

To differentiate contributions of different materials on the SWASV current, we investigated SWASV current of 40 ppb Pb(II) and Cd(II) with various electrodes (i.e., bare GCE, rGO/GCE, Nafion/GCE, $(BiO)_2CO_3$-rGO/GCE and $(BiO)_2CO_3$-rGO-Nafion/GCE) (Figure 14A). Bare GCE showed the weakest SWASV stripping responses of Pb(II) and Cd(II), meaning it possessed the lowest sensitivity. Although rGO/GCE possessed higher surface area, and lower faradaic charge transfer resistances (R_{ct}) than those of bare GCE, we observed little enhancement of SWASV current with rGO/GCE (Figure 14A), indicating that the impacts of high surface area and low R_{ct} were limited. In contrast, the Nafion/GCE showed a much higher SWASV current than that of bare GCE (Figure 14A), which is because Nafion possesses high cation-exchange ability and could enhance the absorption of HMs. In addition, $(BiO)_2CO_3$-rGO/GCE showed similar enhanced SWASV current to that of Nafion/GCE (Figure 14A), which is because Bi has ability to form alloys with HMs.[42] These observations indicated that enhanced surface area and decreased R_{ct} were not determined factors controlling SWASV current, while facilitated absorption due to high ion-exchange ability and the ability of Bi to form alloys with HMs play a more important role. These observations corresponded well with the fact that $(BiO)_2CO_3$-rGO-Nafion/GCE showed the highest SWASV current despite its higher R_{ct} and lower electrochemical surface area (135.2 mm^2 vs. 219.4 mm^2) than that of $(BiO)_2CO_3$-

rGO/GCE. Overall, we speculate the highest current shown by $(BiO)_2CO_3$-rGO-Nafion/GCE were due to synergistic effect of rGO, $(BiO)_2CO_3$ and Nafion. Firstly, the presence of rGO in the composite increased the conductivity and effective specific surface. Secondly, $(BiO)_2CO_3$ facilitated the preconcentration of Pb(II) and Cd(II) due to its ability to form multicomponent alloy with HMs, which makes them reduced easily. Last but not least, the presence of Nafion improved the structural stability and the affinity of HMs due to its high cation exchange capacity.

To evaluate the performances of $(BiO)_2CO_3$-rGO-Nafion/GCE, we made calibration curves for 1-60 ppb Cd(II) and Pb(II) in DI water with SWASV (Figure 14B). Because mutual interference between Pb(II) and Cd(II) could be a serious issue in ASV detections, we confirmed that there was little mutual interference between detections of Pb(II) and Cd(II) with $(BiO)_2CO_3$-rGO-Nafion/GCE. As shown in Figure 14B, the response peaks of Cd(II) and Pb(II) increased linearly with increasing concentrations of these HMs. The calibration curves of target HMs were obtained with the well-defined stripping peaks observed at around −0.80 V for Cd(II) and −0.55 V for Pb(II). The corresponding fitting equations were $y = 0.177x + 1.89$ (x: ppb, y: μA, 1 to 60 ppb, $r = 0.987$) for Cd(II), and $y = 0.126x + 1.038$ (x: ppb, y: μA, 1 to 60 ppb, $r = 0.992$) for Pb(II), as shown in the Figure 14B(b) and Figure 14B(c). The limits of detection (LOD) were calculated as 0.24 ppb for Pb(II) and 0.16 ppb for Cd(II) (LOD = 3*StDev/Slope).

In order to further evaluate the reproducibility and stability, fourteen repetitive measurements of the SWASV current of 50 ppb Cd (II) and 25 ppb Pb(II) were carried out. As shown in Figure 14C, the stripping signals of the fourteen tests showed a low relative standard deviation (RSD) of 1.034% for Cd (II) and 1.167% for Pb (II), indicating that the developed $(BiO)_2CO_3$-rGO-Nafion/GCE was a robust electrode. In addition, Figure 14D shows that up to 10 ppm Na(I), K(I), Fe(II), Mn(II), Mg(II), and Ca(II) had little impact on the detections of 10 ppb Cd(II) and Pb(II), while 10 ppm Zn(II) caused 40.49% and 16.58% current increase for Cd(II) and Pb(II), respectively. However, it is reasonable to assume that Zn(II) would not significantly influence the detections of Pb(II) and Cd(II) in natural waters or MWW because the concentrations of Zn(II) in these waters are generally low. In order to estimate the practicality of the proposed $(BiO)_2CO_3$-rGO-Nafion/GCE for the analysis of Pb(II) and Cd(II), several synthetic river water samples simulating Yamuna River were firstly tested. Without any pretreatment, the average recoveries of Cd(II) and Pb(II) were calculated to be 100.42% and 99.98%, respectively.

Overall, proposed $(BiO)_2CO_3$-rGO-Nafion/GCE showed satisfying performances, including high sensitivity, good stability, and high resistances to interferences, in relatively simple conditions (DI water and river water).

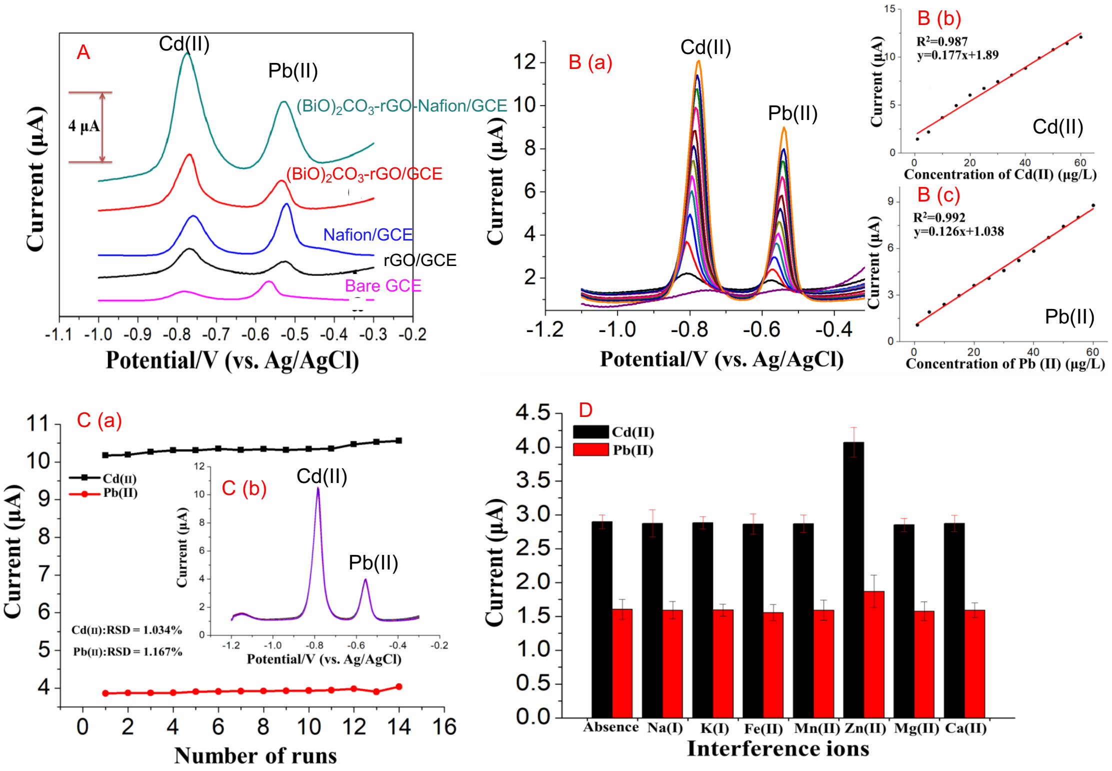

Figure 14. A) The SWASV curves of 40 ppb Pb(II) and Cd(II) with bare GCE, rGO/GCE, Nafion/GCE, $(BiO)_2CO_3$-rGO/GCE, and $(BiO)_2CO_3$-rGO-Nafion/GCE, B) (a) SWASV for 1, 5, 10, 15, 20, 25, 30, 35, 40, 45, 50, 55, and 60 ppb Cd(II) and Pb(II) with $(BiO)_2CO_3$-rGO-Nafion/GCE; (b) and (c) shows the calibration curves for Cd(II), and Pb respectively. C) shows the stability of stripping current for up to 14 times detections of 50 ppb Cd (II) and 25 ppb Pb(II) with $(BiO)_2CO_3$-rGO-Nafion/GCE, and D) shows the impacts of interference ions on the detections of 10 ppb Pb(II) and Cd(II) by $(BiO)_2CO_3$-rGO-Nafion/GCE.

Mutual interference could be a serious problem in the simultaneous detection of Cd(II) and

Pb(II). Therefore, an individual measurement of Pb(II) or Cd(II) was carried out by fixing the concentration of one of these ions whereas the concentration of another one was changed in the meanwhile. As seen in Figure 15A, with the concentration of Cd(II) fixed at 40 ppb, the stripping peaks of Pb(II) increased linearly with an increase of concentration of Pb(II) while the stripping peak of Cu (II) kept constant. The similar results could be obtained with increasing the concentration of Cd(II) but keeping the concentration of Pd(II) constant at 25 μg/L, as shown in Figure 15B. This revealed that the stripping peaks of Cd(II) and Pb(II) were completely independent with each other in the binary mixtures of these ions.

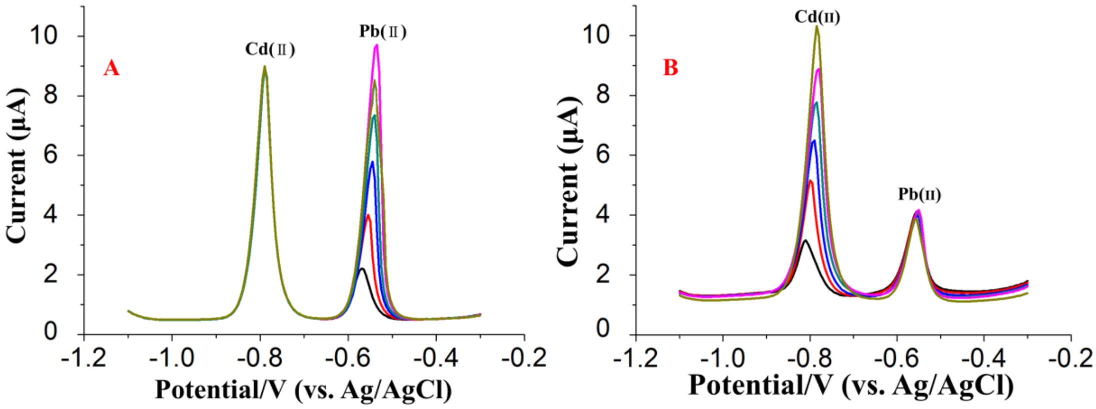

Figure 15. SWASV curves at $(BiO)_2CO_3$-rGO-Nafion/GCE in 0.2 M acetate buffer solution (pH 5.0) containing (a) different concentrations (10-60 ppb) of Pb(II) in the presence of 40 ppb Cd(II), (b) different concentrations (10-60 ppb) of Cd(II) in the presence of 25 ppb Pb(II).

3.2.3 Summary of electrode fabrication and test

In this part, a novel electrochemical sensors for the simultaneous detection of Pb(II) and Cd(II) in water samples was developed based on $(BiO)_2CO_3$-rGO-Nafion/GCE. The analytical and microscopic features of the proposed $(BiO)_2CO_3$-rGO-Nafion/GCE were characterized by SEM, EDX, FTIR, Raman, XRD, CV, EIS and SWASV, which showed that the synergistic effect of $(BiO)_2CO_3$, rGO, Nafion resulted in a much larger specific surface area, better electrical conductivity and higher catalytic ability than the bare electrode, and more Pb(II) and Cd(II) were electrodeposited on the surface of the electrode. The proposed $(BiO)_2CO_3$-rGO-Nafion/GCE achieved a low limit of detection, a high sensitivity and a good stability for the SWASV analysis of Pb(II) and Cd(II).

In addition, an effective sensitive interface was designed using AuNPs decorated with Fe_3O_4NPs embedded in IL for the determination of As(III) at a trace level based on adsorbent-assisted in-situ electrocatalysis. The analytical, spectroscopic and microscopic features of the proposed Fe_3O_4-Au-IL/GCE characterization by XRD, EDX, TEM, SEM, EIS SWASV, and CV showed that the combined effect of AuNPs, Fe_3O_4 and IL resulted in a much better electrical conductivity, larger specific surface area and higher catalytic ability than the bare electrode. Moreover, several synthetic water samples were tested to further verify the practicability of the proposed platform. The results showed that Fe_3O_4-Au-IL/GCE can be successfully applied to the analysis of As(III) in synthetic river and wastewater samples without any sample pretreatment procedures, which suggested that it could be further applied to heavy metal analysis in real samples.

3.3 Identify Pretreatment Methods for Metal Detection using ASV

3.3.1 Acidification coupled with (BiO)2CO3-rGO-Nafion/GCE to detect low-concentration metals

Figure 16 and Figure 17 show the impact of acidification (pH 1) on the detection of low-concentration Cd (i.e., 3.5 ppb) and Pb (i.e., 12.5 ppb) by ASV (the results in Figure 16 are normalized to the concentrations measured using ICP-MS, while Figure 17 shows the absolute value measured by ASV and ICP-MS). While ASV was able to detect only 64% and 48% of Pb in synthetic and real secondary treatment wastewater, respectively, in untreated samples, acidification dramatically enhanced ASV detection of Pb, enabling ASV to achieve similar detection results to ICP-MS in both synthetic raw wastewater (101% ± 14% in Figure 16 and Figure 17) and real secondary treatment wastewater (102% ± 21% in Figure 16 and Figure 17); these results are largely in-line with data calculated by Visual MINTEQ, which predicted that 85% of Pb should be present in its ionic form at pH = 1 (Figure 2E). It is worth noting that despite its success at pH =1, this model severely underestimated free Pb (i.e., ASV detectable Pb) at pH = 7. This underestimation of free metals was also reported in another study.[43] Previous studies have reported that acidic conditions can facilitate metal release from humic acid as well.[44] However, the minimum pH set by other studies are generally larger than 2, which could not completely release metals.[44-47] The improved ASV detection of Pb is attributed to the destruction of the Pb-NOM complex, due to protonation of carboxylic binding sites on NOM. In the synthetic wastewater, the main NOM was humic acid, which precipitated significantly (based on visual examination) when the pH was decreased to 1. In addition to humic acid, real secondary effluent likely contained many other organic molecules, including fulvic acid, synthetic organic compounds, and microbial products.[48] It has been reported that DOM in some wastewater effluents is composed primarily of fulvic acid.[49] Overall, acidification results indicate that Pb(II) is bound to carboxylic groups in NOM or inorganic particles, which generally cannot pass through 5 kDa membranes. This is supported by a fact that most of complexed Pb(II) in wastewater is rejected by 5 kDa membranes.[50]

Acidification had only a slight impact on Cd detection by ASV in both synthetic wastewater (from 56% ± 20% to 69% ± 5% in Figure 16C and Figure 17C) and real secondary treatment wastewater (from 32% ± 9% to 44% ± 1% in Figure 16 and Figure 17D). The % detection of Cd by ASV in synthetic wastewater following acid treatment corresponds well with the Visual MINTEQ model predictions; the model predicted that at pH 1, 71% of Cd would be in ionic form (ASV results yielded 69% ± 5%). However, the model showed that Cd is able to complex with Cl^- at low pH (Figure 16E). This complexation has been shown to shift the half-wave potential of Cd.[51] However, we didn't observe a distinguishable shift in the Cd signal. While decreasing the pH to 1 was supposed to dissolve the majority of inorganic substances, our results show that acidification had a relatively minor impact on the amount of Cd available for ASV detection, suggesting that the majority of Cd(II) is not bound to inorganic particles or carboxylic groups in NOM, which corresponds well with previous research stating that compared to Pb(II), it is harder for Cd(II) to complex with NOM.[52] We speculate that Cd(II) is bound to non-humic DOC, which generally has a lower molecular weights than NOM. This speculation was supported by the fact that most of the complexed Cd in wastewater could pass through membranes with pore size of 5 kDa.[50]

Overall, it was found that acidification to pH 1 enabled the efficient detection by ASV of trace Pb concentrations (12.5 ppb) in both synthetic and real wastewater, however, it failed to make trace (3.5 ppb) Cd detectable by ASV.

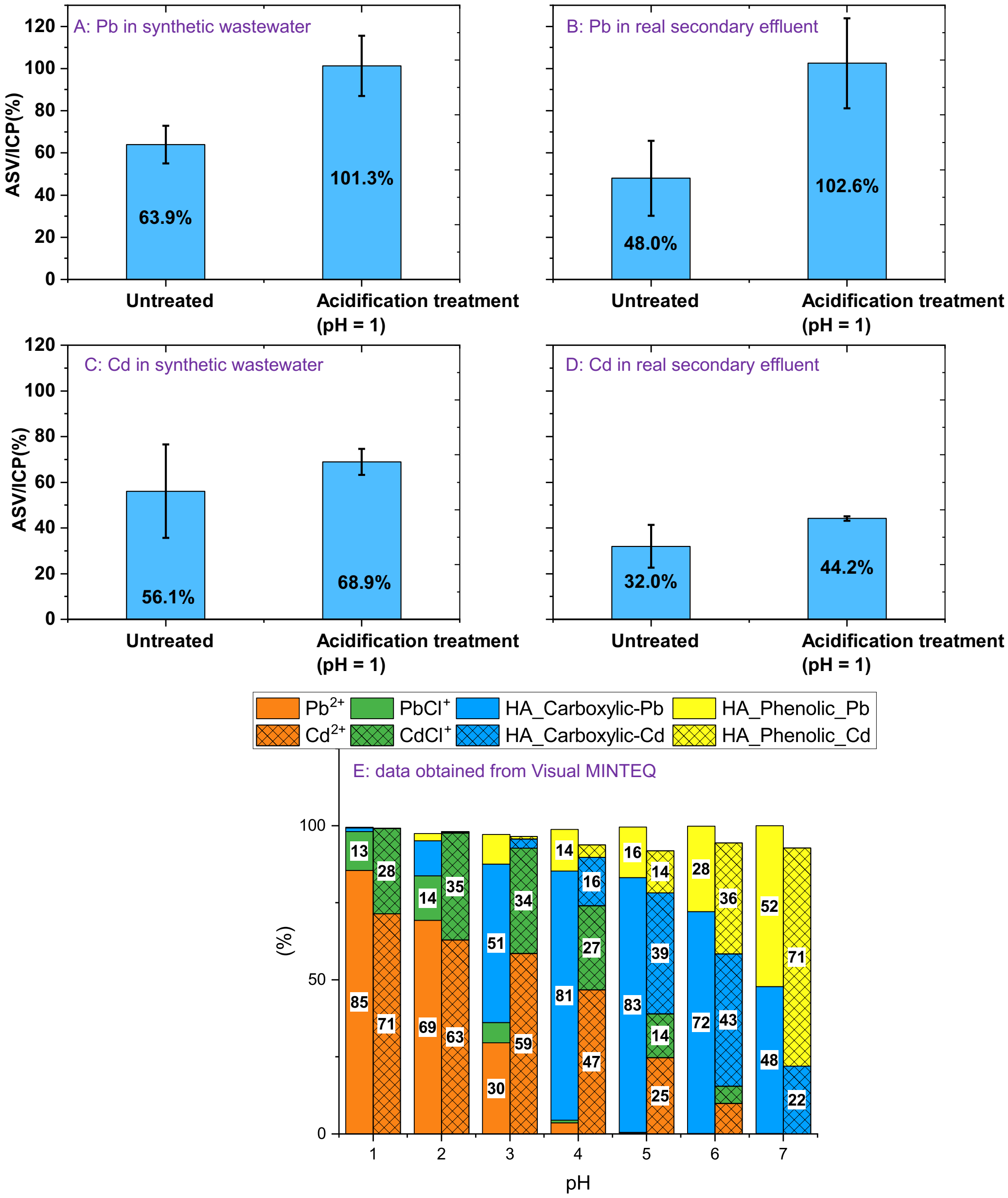

Figure 16. The detection of trace Pb (A, B) and Cd (C, D) by ASV and ICP-MS in synthetic wastewater (A, C) and real secondary treatment wastewater (B, D) before and after acidification; E shows the influence of pH on the metal speciation distribution in synthetic wastewater predicted by Visual MINTEQ 3.1; Fractions lower than 3 % were ignored and fractions lower than 10% were not labeled with exact number in this figure. NICA-Donnan model was chosen to calculate the complex between metal and humic substances.

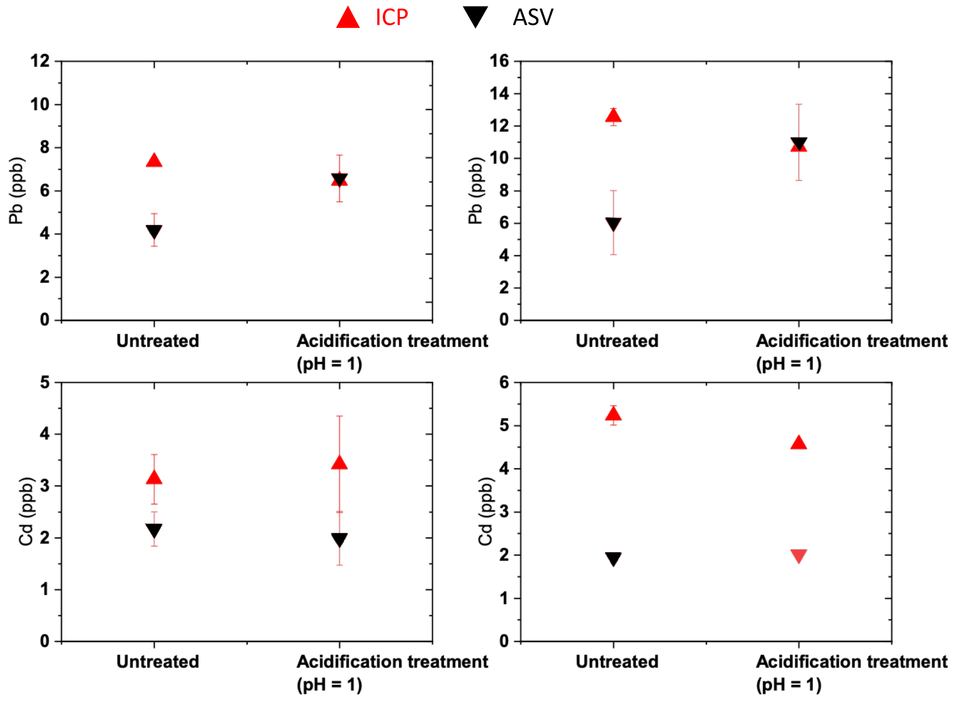

Figure 17. The absolute value of trace Pb (A, B) and Cd (C, D) measured by ASV and ICP-MS in synthetic wastewater (A, C) and real secondary treatment wastewater (B, D) before and after acidification;

3.3.2 VUV/H_2O_2 coupled with (BiO)2CO3-rGO-Nafion/GCE

Figure 18 and Figure 19 (the results in Figure 18 are normalized to the concentrations measured using ICP-MS, while Figure 19 shows the absolute value measured by ASV and ICP-MS) show the ASV and ICP-MS detection of high-concentration metals (i.e., 100 ± 9 ppb Cd and 1058 ± 113 ppb Pb) in synthetic wastewater samples before and after VUV/H_2O_2 treatment. A 0.5 h VUV/H_2O_2 treatment significantly enhanced the amount of metals available for ASV detection (from 37% ± 8% to 92% ± 4% for Cd and from 48% ± 11% to 97% ± 0.7% for Pb), indicating that VUV/H_2O_2 is a robust process to release high-concentration metals (Figure 18A-B and Figure 19 A-B). It is noted that the pH of the solution after treatment was

7.2 ± 0.3, a level that HMs are not expected to be complexed with Cl^-, but rather be primarily complexed with organic matter (Figure 18E). However, the presence of residual H_2O_2 remaining in the solution was found to interfere with Cd detection by ASV (Figure 18A and Figure 19A). Therefore, to eliminate this interference, we added 1200 ppm Na_2SO_3 to quench residual H_2O_2, which enabled ASV to achieve comparable results to ICP-MS (Figure 18A and Figure 19A). Interestingly, ASV detection of high-concentration Pb was insensitive to residual H_2O_2 (Figure 18B and Figure 19B). We speculate that this is because the concentration of Pb in this case was high enough to have a sufficiently high signal-to-noise ratio, and thus be resistant to the presence of residual H_2O_2. However, the impact of residual H_2O_2 on the detection of low-concentration Pb was observed, and quenching of H_2O_2 was necessary (more on this below).

VUV/H_2O_2 is a complex photolysis process that can involve multiple reactive pathways responsible for the degradation of DOC.[53, 54] Overall, VUV/H_2O_2 mechanisms can be classified into direct photolysis (i.e., by VUV), indirect photolysis (by radicals induced by VUV),[54] and direct oxidation by the H_2O_2 or ozone [55] (ozone can be generated by VUV irradiation).[56] Under VUV (i.e., UV with wavelength = 185 nm), ozone would produced from oxygen.[56]

$O_2 + hv_{185nm} \rightarrow 2\ O$

$O\ \ + O_2 \rightarrow O_3$

The produced ozone could oxidize organics directly, however, ozone would form hydroxyl radicals under UV radiation in aqueous solutions.[56]

$O_3 + H_2O + h\nu_{254\ \mathrm{nm}} \rightarrow H_2O_2 + O_2$

$H_2O_2 + h\nu_{254\ \mathrm{nm}} \rightarrow 2\ {\bullet}OH$

Hydroxyl radicals (•OH) are non-target oxidants that are powerful to degrade organics.[56]

After validation of the effectiveness of VUV/H_2O_2 pretreatment for the detection of high-concentration HMs, we further evaluated the effectiveness of VUV/H_2O_2 on low-concentration HM samples. With a 1-h VUV/H_2O_2 treatment, 103% ± 4% and 89% ± 9% of Cd was detected by ASV in synthetic and real secondary treatment samples, respectively (Figure 18C, E). This is because Cd(II) ions are likely bound to small organic molecules, evidenced by the fact that most of the complexed Cd(II) in wastewater could pass through membranes with a pore size of 5 kDa.[50] These small organic molecules are more readily mineralized by the VUV/H_2O_2 treatment compared to NOM,[57] which releases the Cd(II), making it available to ASV detection.

However, some loss of Cd was observed after VUV/H_2O_2 treatment in both ICP-MS and ASV measurements, where the total amount of Cd in real secondary treatment effluent decreased 0.22 ± 0.01 μg (from 4.46 ± 0.09 ppb to 2.22 ± 0.23 ppb in 100 mL solution) (Figure 19E). It is noted that similar Cd loss (i.e., from 4.30 ± 0.08 ppb to 2.48 ± 0.07 ppb in 100 mL solution) was also observed in the control group (i.e., solutions containing only DI water and cadmium), indicating that these errors were systematic. Similar losses were observed in real tertiary treated wastewater (decrease from 4.21 ± 0.02 ppb to 2.34 ± 0.43 ppb), with ASV achieving similar results with ICP-MS after VUV/H_2O_2 (Figure 19). These systematic errors are likely because of Cd sorption on PVC reactor.[58] Therefore, we conclude that VUV/H_2O_2 is an effective pre-treatment step for enabling Cd detection by ASV. 1 h VUV/H_2O_2 pretreatment slightly increased the amount of Pb available for ASV detections in synthetic wastewater (from 49.6% ± 5% to 65% ± 3% in Figure 18D and Figure 19D) and real secondary effluent (from 20% ± 5% to 40% ± 9% Figure 18F and Figure 19F). To explore whether adsorption to inorganic particles was preventing the complete detection of trace Pb concentrations, HNO_3 was used to adjust the solution pH to 2 after the VUV/H_2O_2 treatment. However, the acidic pH led to a decreased amount of detectable Pb and Cd available for ASV detection (Figure 18E, F and Figure 19E, F). We speculate that the impaired metal detection at low pH resulted from interferences from SO_2, which is electrochemically active [59]. SO_2 can be produced from the hydrolysis of HSO_3^- (originating from Na_2SO_3 used to quench H_2O_2) at low pH (pKa1 for SO_2/H_2SO_3 is 1.91). As a result, it is impractical follow the VUV/H_2O_2 treatment with acidification.

Overall, 30-min VUV/H_2O_2 is a robust technique to make high-concentration (100 ppb) Cd and (1058 ppb) Pb available for ASV detection. Furthermore, although a systematic error was observed in VUV/H_2O_2 treated samples containing trace (3~4 ppb) Cd, this systematic error can be eliminated by using inert reactor materials that do not absorb Cd(e.g., glass material).

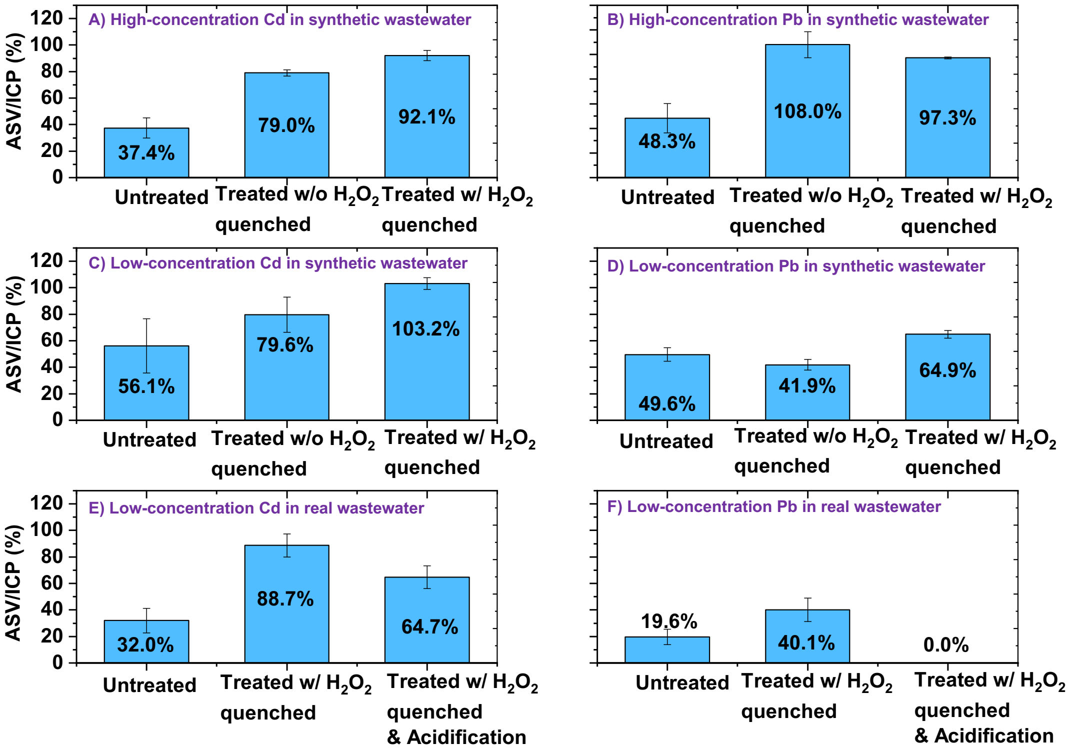

Figure 18. The detection of high (A, B) and low concentration(C, D, E, F) of Pb (B, D, F) and Cd (A, C, E) by ASV and ICP-MS in synthetic wastewater and real secondary effluent before and after VUV/H_2O_2 treatment; Photolysis conditions: pH was around 7, initial H_2O_2 concentration was 1 g/L, temperature was 25 ℃ (temperature increased to around 40 ℃ during photolysis due to heat dissipated from the lamp); 0.5-h photolysis for high-concentration metals, 1-h photolysis for low-concentration metals; Residue H_2O_2 was quenched by Na_2SO_3.

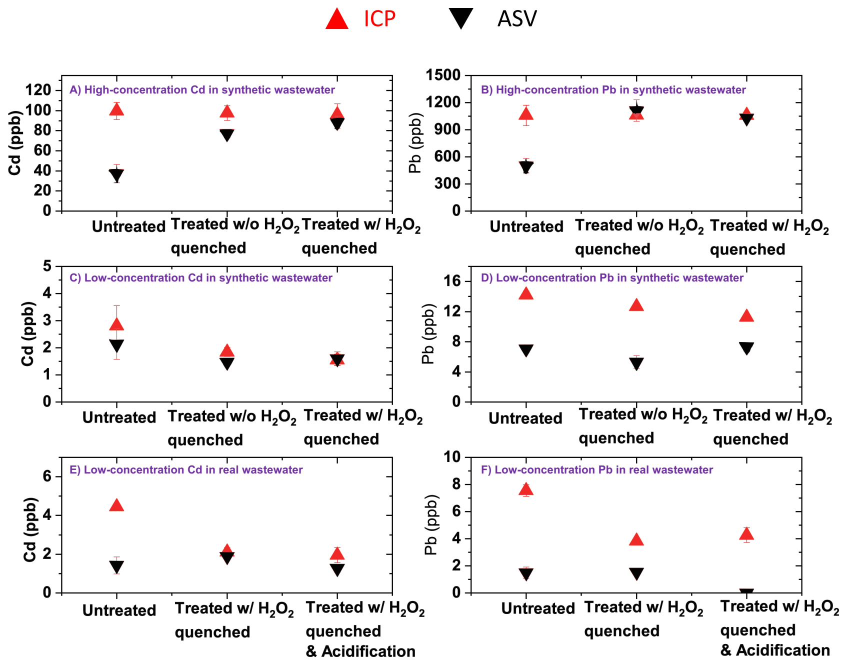

Figure 19. The absolute value of high (A, B) and low concentration(C, D, E, F) of Pb (B, D, F) and Cd (A, C, E) by ASV and ICP-MS in synthetic wastewater and real secondary effluent before and after VUV/H_2O_2 treatment; Photolysis conditions: pH was around 7, initial H_2O_2 concentration was 1 g/L, temperature was 25 ℃ (temperature increased to around 40 ℃ during photolysis due to heat dissipated from the lamp); 0.5-h photolysis for high-concentration metals, 1-h photolysis for low-concentration metals; Residue H_2O_2 was quenched by Na_2SO_3.

3.3.3 Summary of pretreatment methods

ASV is an attractive on-site, low-cost metal detection technique capable of performing frequent and highly accurate measurements with little user input (i.e., the system can be readily automated). We demonstrated that appropriate pre-treatment (acidification for Pb and VUV/H_2O_2 + Na_2SO_3 quenching for Cd) enables the sensitive detection of Cd and Pb in complex waste stream down to low ppb levels. Detection was enabled by using novel electrodes that are easily processable and scalable, and enabled very low LODs (0.24 and 0.16 ppb for Cd and Pb). The deployment of the method described here (pretreatment + ASV) has the potential of enabling the low-cost and frequent detection of HMs in complex wastewater streams, which will reduce the reliance on expensive and time-consuming ICP-based methods. The low-cost and frequent monitoring of HMs in wastewater could enable its more widespread use in various recycling activities, such as cooling and agricultural irrigation.

3.4 ASV device based on Python and Arduino

Figure 20 shows the ASV measurement graphical user interface (GUI) written in Python 2.7, which is a free open-source language. This system requires 3 springy pumps to control the addition of chemicals and one UV lamp to conduct photolysis. Springy pumps are controlled directly by Python, while the UV lamp is controlled by Arduino Uno (Figure 21), which is an open-source hardware and costs around $20. This system could do pretreatment and ASV analysis automatically.

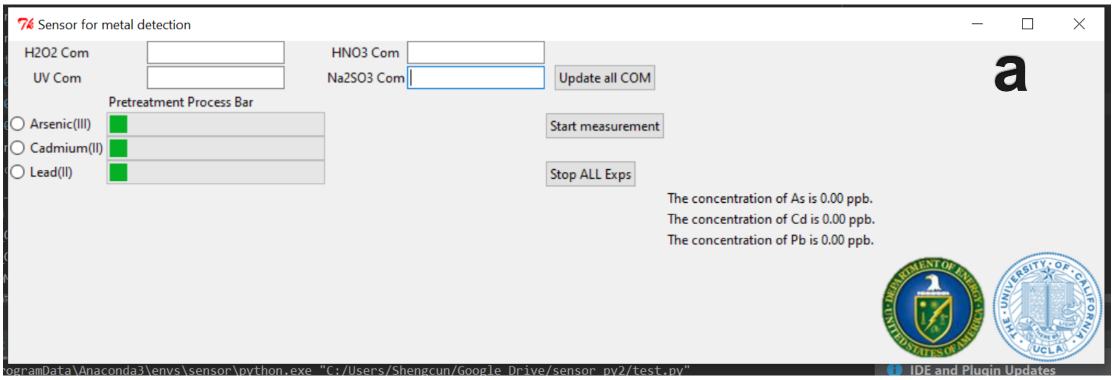

```
The concentration of As is 0.00 ppb.
The concentration of Cd is 0.00 ppb.
The concentration of Pb is 0.00 ppb.
```

```
ogramData\Anaconda3\envs\sensor\python.exe "C:/Users/Shengcun/Google Drive/sensor py2/test.py"
```

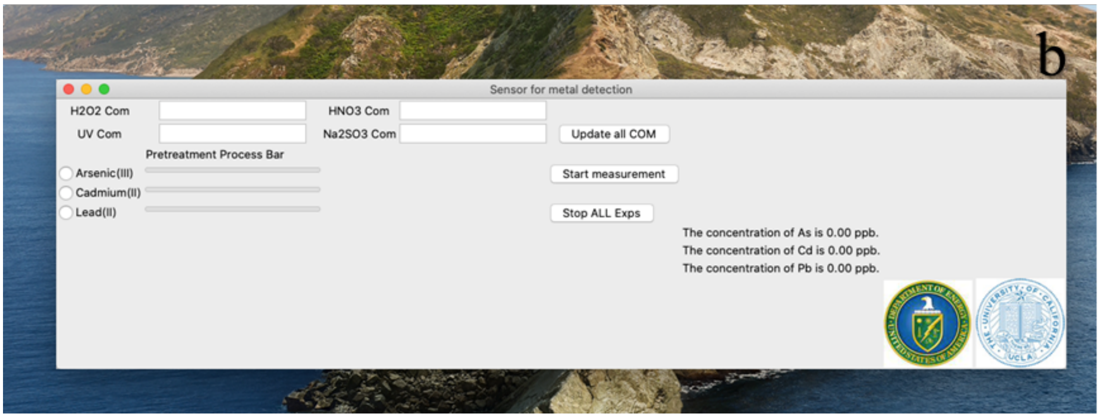

The concentration of As is 0.00 ppb.
The concentration of Cd is 0.00 ppb.
The concentration of Pb is 0.00 ppb.

Figure 20. The GUI for metal detection by ASV operated on a) Windows 10 and b) Mac OS Catalina (Version 10.15).

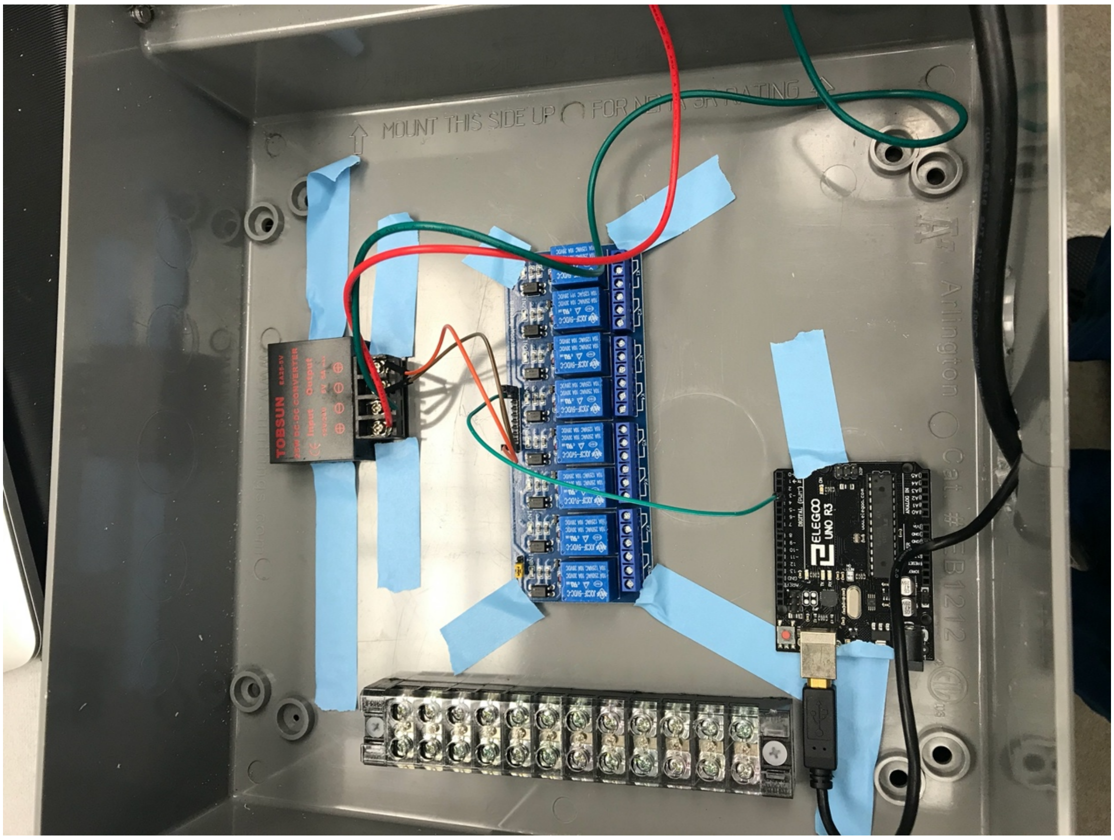

Figure 21. Arduino based open-source hardware

4.Conlcusion

Firstly, we evaluated how different wastewater characteristics impact the speciation and form of heavy metals (Pb, Cd, and As), as the evolution of metal size distribution and partitioning throughout the WWTT is of paramount importance for developing metal detection and metal removal techniques. Cd was found to be highly mobile, with the fraction of dissolved Cd gradually increasing throughout the WWTT. As(III) was also highly mobile, with its size distribution and partitioning remaining largely steady, except when $FeCl_3$ was used as a flocculation agent, which led to the formation of arsenic/iron complexes. However, Pb was found primarily in complex forms or adsorbed onto inorganic particulates. The WWTT had little impact on the size and partitioning of Pb, except that the formation of the Pb/iron complex occurred after flocculation with $FeCl_3$. An increase of water hardness slightly increased the metals in the dissolved fraction. Overall, metal characterization work provides insight into the evolution of metals throughout the WWTT, offering guidance to users and researchers regarding their treatment and detection.

Secondly, we fabricated innovative electrodes for ASV measurements of As(III), Pb(II), and Cd(II). The electrode materials have been characterized for their structure by spectroscopy (UV-vis, FTIR, Raman and XRD), microscopy (SEM and TEM) and calorimetry (TGA and DSC) to look into the phase, morphology and defects. The prepared Fe_3O_4-Au nanocomposite was embedded in ionic liquid (IL) and applied for the modification of glassy carbon electrode (GCE) for the electrochemical detection of As(III) in water. By combining the excellent catalytic properties of the AuNPs with the high adsorption capacity of the tiny Fe_3O_4NPs towards As(III), as well as the good conductivity of IL, the Fe_3O_4-Au-IL nanocomposite shows excellent performance in the square wave anodic stripping voltammetry detection of As(III). Under the optimized conditions, a linear range of 1 to 100 µg/L was achieved with a detection limit of 0.22 µg/L (S/N = 3), and no interference from 100-fold higher concentrations of a wide variety of cations and anions found in water. A very low residual standard deviation of 1.16% confirmed the high precision/reproducibility of As(III) analysis and the reliability of the Fe_3O_4-Au-IL sensing interface. In addition, bismuth subcarbonate $(BiO)_2CO_3$-reduced graphene oxide nanocomposite incorporated in Nafion matrix ($(BiO)_2CO_3$-rGO-Nafion) was synthesized and further applied for the first time in the sensitive detection of Pb(Ⅱ) and Cd(Ⅱ) by the square wave anodic stripping voltammetry (SWASV). the $(BiO)_2CO_3$-rGO/Nafion nanocomposite modified glassy carbon electrode ($(BiO)_2CO_3$-rGO-Nafion/GCE) achieves low detection limits of 0.24 µg/L for Pb(Ⅱ) and 0.16 µg/L for Cd(Ⅱ), in the linear range of 1.0-60 µg/L, and shows some excellent performance, such as high stability, good selectivity and sensitivity.

Finally, we have developed a processing method that enables the detection of Pb(II) and Cd(II) in MWW using ASV, and fabricated automatic ASV device based on Python and Arduino. In this process, HM-containing MWW is pre-treated by either vacuum ultraviolet (VUV)/H_2O_2 (Cd) or a strong acid (Pb), which releases the bound HMs. HMs are then accurately detected and quantified using ASV by utilizing a bismuth subcarbonate/reduced graphene oxide nanocomposite incorporated in a Nafion matrix electrode. The resulting sensing process is able to detect trace concentrations of Cd and Pb in both synthetic and real MWW samples. Detection results were benchmarked against state-of-the-art metal detection methods, and were found to be highly accurate (>88%). This pre-treatment and detection method enables utilities and end-users to frequently monitor HM concentrations in complex streams.

Reference:

[1] R. Buzier, M.-H. Tusseau-Vuillemin, C.M. dit Meriadec, O. Rousselot, J.-M. Mouchel, Trace metal speciation and fluxes within a major French wastewater treatment plant: Impact of the successive treatments stages, Chemosphere, 65 (2006) 2419-2426.

[2] A.J. Hargreaves, P. Vale, J. Whelan, C. Constantino, G. Dotro, P. Campo, E. Cartmell, Distribution of trace metals (Cu, Pb, Ni, Zn) between particulate, colloidal and truly dissolved fractions in wastewater treatment, Chemosphere, 175 (2017) 239-246.

[3] G. Sheng, S. Wang, J. Hu, Y. Lu, J. Li, Y. Dong, X. Wang, Adsorption of Pb (II) on diatomite as affected via aqueous solution chemistry and temperature, Colloids and Surfaces A: Physicochemical and Engineering Aspects, 339 (2009) 159-166.

[4] I.A. Worms, Z. Al-Gorani Szigeti, S. Dubascoux, G. Lespes, J. Traber, L. Sigg, V.I. Slaveykova, Colloidal organic matter from wastewater treatment plant effluents: Characterization and role in metal distribution, Water Res, 44 (2010) 340-350.

[5] T. Wang, W. Liu, L. Xiong, N. Xu, J. Ni, Influence of pH, ionic strength and humic acid on competitive adsorption of Pb(II), Cd(II) and Cr(III) onto titanate nanotubes, Chemical Engineering Journal, 215-216 (2013) 366-374.

[6] M. Sadiq, T.H. Zaidi, A.A. Mian, Environmental behavior of arsenic in soils: Theoretical, Water, Air, & Soil Pollution, 20 (1983) 369-377.

[7] G. Zhang, J. Qu, H. Liu, R. Liu, R. Wu, Preparation and evaluation of a novel Fe-Mn binary oxide adsorbent for effective arsenite removal, Water Res, 41 (2007) 1921-1928.

[8] R.L. Vaughan, Jr., B.E. Reed, Modeling As(V) removal by a iron oxide impregnated activated carbon using the surface complexation approach, Water Res, 39 (2005) 1005-1014.

[9] A.J. Hargreaves, P. Vale, J. Whelan, L. Alibardi, C. Constantino, G. Dotro, E. Cartmell, P. Campo, Correction to: Coagulation–flocculation process with metal salts, synthetic polymers and biopolymers for the removal of trace metals (Cu, Pb, Ni, Zn) from municipal wastewater, Clean Technologies and Environmental Policy, 20 (2018) 1119-1119.

[10] H.G. Brown, C.P. Hensley, G.L. McKinney, J.L. Robinson, Efficiency of Heavy Metals Removal in Municipal Sewage Treatment Plants, Environmental Letters, 5 (2009) 103-114.

[11] M.E. Goldstone, C. Atkinson, P.W.W. Kirk, J.N. Lester, The behaviour of heavy metals during wastewater treatment III. Mercury and arsenic, Science of The Total Environment, 95 (1990) 271-294.

[12] R.M. Sterritt, M.J. Brown, J.N. Lester, Metal removal by adsorption and precipitation in the activated sludge process, Environmental Pollution Series A, Ecological and Biological, 24 (1981) 313-323.

[13] G.P. Sheng, J. Xu, H.W. Luo, W.W. Li, W.H. Li, H.Q. Yu, Z. Xie, S.Q. Wei, F.C. Hu, Thermodynamic analysis on the binding of heavy metals onto extracellular polymeric substances (EPS) of activated sludge, Water Res, 47 (2013) 607-614.

[14] M. Brown, J. Lester, Metal removal in activated sludge: the role of bacterial extracellular polymers, Water Research, 13 (1979) 817-837.

[15] G. Guibaud, N. Tixier, A. Bouju, M. Baudu, Relation between extracellular polymers' composition and its ability to complex Cd, Cu and Pb, Chemosphere, 52 (2003) 1701-1710.

[16] P. Venkateswaran, S. Vellaichamy, K. Palanivelu, Speciation of heavy metals in electroplating industry sludge and wastewater residue using inductively coupled plasma, International Journal of Environmental Science & Technology, 4 (2007) 497-504.

[17] M. Chen, X.M. Li, Q. Yang, G.M. Zeng, Y. Zhang, D.X. Liao, J.J. Liu, J.M. Hu, L. Guo, Total concentrations and speciation of heavy metals in municipal sludge from Changsha, Zhuzhou and Xiangtan in middle-south region of China, J Hazard Mater, 160 (2008) 324-329.

[18] C. Plaza, G. Brunetti, N. Senesi, A. Polo, Molecular and Quantitative Analysis of Metal Ion Binding to Humic Acids from Sewage Sludge and Sludge-Amended Soils by Fluorescence Spectroscopy, Environmental Science & Technology, 40 (2006) 917-923.

[19] F. Ahmadipour, N. Bahramifar, S. Mahmood Ghasempouri, Fractionation and mobility of cadmium and lead in soils of Amol area in Iran, using the modified BCR sequential extraction method, Chemical Speciation & Bioavailability, 26 (2014) 31-36.

[20] F. Stevenson, Nature of divalent transition metal complexes of humic acids as revealed by a modified potentiometric titration method, Soil Science, 123 (1977) 10-17.

[21] C. Moreno-Castilla, M.A. Alvarez-Merino, M.V. Lopez-Ramon, J. Rivera-Utrilla, Cadmium ion adsorption on different carbon adsorbents from aqueous solutions. Effect of surface chemistry, pore texture, ionic strength, and dissolved natural organic matter, Langmuir, 20 (2004) 8142-8148.

[22] T.S. Choong, T. Chuah, Y. Robiah, F.G. Koay, I. Azni, Arsenic toxicity, health hazards and removal techniques from water: an overview, Desalination, 217 (2007) 139-166.

[23] S. Hafeznezami, A.G. Zimmer-Faust, D. Jun, M.B. Rugh, H.L. Haro, A. Park, J. Suh, T. Najm, M.D. Reynolds, J.A. Davis, T. Parhizkar, J.A. Jay, Remediation of groundwater contaminated with arsenic through enhanced natural attenuation: Batch and column studies, Water Res, 122 (2017) 545-556.

[24] N. Ma, A.A. Rouff, Influence of pH and oxidation state on the interaction of arsenic with struvite during mineral formation, Environmental science & technology, 46 (2012) 8791-8798.

[25] H.A. Andrianisa, A. Ito, A. Sasaki, J. Aizawa, T. Umita, Biotransformation of arsenic species by activated sludge and removal of bio-oxidised arsenate from wastewater by coagulation with ferric chloride, Water Res, 42 (2008) 4809-4817.

[26] M.-J. Kim, J. Nriagu, S. Haack, Carbonate ions and arsenic dissolution by groundwater, Environmental Science & Technology, 34 (2000) 3094-3100.

[27] D.B. Senn, J.E. Gawel, J.A. Jay, H.F. Hemond, J.L. Durant, Long-term fate of a pulse arsenic input to a eutrophic lake, Environmental science & technology, 41 (2007) 3062-3068.

[28] R.S. Rathore, B. Khangarot, Effects of water hardness and metal concentration on a freshwater Tubifex tubifex Muller, Water, Air, and Soil Pollution, 142 (2003) 341-356.

[29] R.J. Martins, R. Pardo, R.A. Boaventura, Cadmium (II) and zinc (II) adsorption by the aquatic moss Fontinalis antipyretica: effect of temperature, pH and water hardness, Water Research, 38 (2004) 693-699.

[30] A. Alpatova, S. Verbych, M. Bryk, R. Nigmatullin, N. Hilal, Ultrafiltration of water containing natural organic matter: heavy metal removing in the hybrid complexation–ultrafiltration process, Separation and Purification Technology, 40 (2004) 155-162.

[31] A. Ahmad, S. Rutten, L. de Waal, P. Vollaard, C. van Genuchten, H. Bruning, E. Cornelissen, A. van der Wal, Mechanisms of arsenate removal and membrane fouling in ferric based coprecipitation–low pressure membrane filtration systems, Separation and Purification Technology, 241 (2020).

[32] A.K. Pandey, S.D. Pandey, V. Misra, Stability constants of metal-humic acid complexes and its role in environmental detoxification, Ecotoxicol Environ Saf, 47 (2000) 195-200.

[33] Y. Xiong, Experimental determination of lead carbonate solubility at high ionic strengths: a Pitzer model description, Monatshefte für Chemie-Chemical Monthly, 146 (2015) 1433-1443.

[34] D. Li, M.B. Muller, S. Gilje, R.B. Kaner, G.G. Wallace, Processable aqueous dispersions of graphene nanosheets, Nat Nanotechnol, 3 (2008) 101-105.

[35] C.d.C.A. Lopes, P.H.J.O. Limirio, V.R. Novais, P. Dechichi, Fourier transform infrared spectroscopy (FTIR) application chemical characterization of enamel, dentin and bone, Applied Spectroscopy Reviews, 53 (2018) 747-769.

[36] R. Kumar, C. Xu, K. Scott, Graphite oxide/Nafion composite membranes for polymer electrolyte fuel cells, Rsc Advances, 2 (2012) 8777-8782.

[37] S. Abdolhosseinzadeh, H. Asgharzadeh, H.S. Kim, Fast and fully-scalable synthesis of reduced graphene oxide, Scientific reports, 5 (2015) 10160.

[38] S. Stankovich, R.D. Piner, S.T. Nguyen, R.S. Ruoff, Synthesis and exfoliation of isocyanate-treated graphene oxide nanoplatelets, Carbon, 44 (2006) 3342-3347.

[39] F. Dong, S.C. Lee, Z. Wu, Y. Huang, M. Fu, W.K. Ho, S. Zou, B. Wang, Rose-like monodisperse bismuth subcarbonate hierarchical hollow microspheres: one-pot template-free fabrication and excellent visible light photocatalytic activity and photochemical stability for NO removal in indoor air, J Hazard Mater, 195 (2011) 346-354.

[40] Z.Q. Li, C.J. Lu, Z.P. Xia, Y. Zhou, Z. Luo, X-ray diffraction patterns of graphite and turbostratic carbon, Carbon, 45 (2007) 1686-1695.

[41] J. Wang, H. Zhang, M.R. Hunt, A. Charles, J. Tang, O. Bretcanu, D. Walker, K.T. Hassan, Y. Sun, L. Šiller, Synthesis and characterisation of reduced graphene oxide/bismuth composite for electrodes in electrochemical energy storage devices, ChemSusChem, 10 (2017) 363-371.

[42] I. Švancara, C. Prior, S.B. Hočevar, J. Wang, A Decade with Bismuth-Based Electrodes in Electroanalysis, Electroanalysis, 22 (2010) 1405-1420.

[43] E.R. Unsworth, K.W. Warnken, H. Zhang, W. Davison, F. Black, J. Buffle, J. Cao, R. Cleven, J. Galceran, P. Gunkel, E. Kalis, D. Kistler, H.P. Van Leeuwen, M. Martin, S. Noel, Y. Nur, N. Odzak, J. Puy, W. Van Riemsdijk, L. Sigg, E. Temminghoff, M.L. Tercier-Waeber, S. Toepperwien, R.M. Town, L. Weng, H. Xue, Model predictions of metal speciation in freshwaters compared to measurements by in situ techniques, Environ Sci Technol, 40 (2006) 1942-1949.

[44] G. Sheng, J. Li, D. Shao, J. Hu, C. Chen, Y. Chen, X. Wang, Adsorption of copper(II) on multiwalled carbon nanotubes in the absence and presence of humic or fulvic acids, J Hazard Mater, 178 (2010) 333-340.

[45] T. Florence, The speciation of trace elements in waters, Talanta, 29 (1982) 345-364.

[46] H.W. Nürnberg, Investigations on heavy metal speciation in natural waters by voltammetric procedures, Fresenius' Zeitschrift für analytische Chemie, 316 (1983) 557-565.

[47] T.M. Florence, Electrochemical approaches to trace element speciation in waters. A review, Analyst, 111 (1986) 489-505.

[48] J. Guo, Y. Peng, J. Guo, J. Ma, W. Wang, B. Wang, Dissolved organic matter in biologically treated sewage effluent (BTSE): Characteristics and comparison, Desalination, 278 (2011) 365-372.

[49] H. Ma, Characterization of isolated fractions of dissolved organic matter from natural waters and a wastewater effluent, Water Research, 35 (2001) 985-996.

[50] S. Ma, S. Poon, A. Mulchandani, D. Jassby, The evolution of metal size and partitioning

throughout the wastewater treatment train, J Hazard Mater, 402 (2021) 123761.

[51] M. Branica, D. Novak, S. Bubić, Application of anodic stripping voltammetry to determination of the state of complexation of traces of metal ions at low concentration levels, Croatica Chemica Acta, 49 (1977) 539-547.

[52] A. Liu, R.D. Gonzalez, Modeling adsorption of copper (II), cadmium (II) and lead (II) on purified humic acid, Langmuir, 16 (2000) 3902-3909.

[53] Q. Zhang, L. Wang, B. Chen, Y. Chen, J. Ma, Understanding and modeling the formation and transformation of hydrogen peroxide in water irradiated by 254 nm ultraviolet (UV) and 185 nm vacuum UV (VUV): Effects of pH and oxygen, Chemosphere, 244 (2020) 125483.

[54] L. Long, Y. Bu, B. Chen, R. Sadiq, Removal of urea from swimming pool water by UV/VUV: The roles of additives, mechanisms, influencing factors, and reaction products, Water Res, 161 (2019) 89-97.

[55] S. Srithep, S. Phattarapattamawong, Kinetic removal of haloacetonitrile precursors by photo-based advanced oxidation processes (UV/H2O2, UV/O3, and UV/H2O2/O3), Chemosphere, 176 (2017) 25-31.

[56] G. Moussavi, M. Mahdavianpour, The selective direct oxidation of ammonium in the contaminated water to nitrogen gas using the chemical-less VUV photochemical continuous-flow reactor, Chemical Engineering Journal, 295 (2016) 57-63.

[57] S.R. Sarathy, M. Mohseni, The impact of UV/H2O2 advanced oxidation on molecular size distribution of chromophoric natural organic matter, Environ Sci Technol, 41 (2007) 8315-8320.

[58] C.M. Rochman, B.T. Hentschel, S.J. Teh, Long-term sorption of metals is similar among plastic types: implications for plastic debris in aquatic environments, PLoS One, 9 (2014) e85433.

[59] J.A. O’Brien, J.T. Hinkley, S.W. Donne, S.E. Lindquist, The electrochemical oxidation of aqueous sulfur dioxide: A critical review of work with respect to the hybrid sulfur cycle, Electrochimica Acta, 55 (2010) 573-591.